Real-time clocking of bimolecular reactions: Application to H+CO$_2$

N. F. Scherer,[a] C. Sipes, R. B. Bernstein,[b] and A. H. Zewail
Arthur Amos Noyes Laboratory of Chemical Physics, California Institute of Technology, Pasadena, California 91125

An experimental methodology is described for the real-time clocking of elementary bimolecular reactions, i.e., timing the process of formation and decay of the collision complex. The method takes advantage of the propinquity of the potential reagents in a binary van der Waals (vdW) "precursor" molecule. An ultrashort pump laser pulse initiates the reaction, establishing the zero-of-time (e.g., by photodissociating one of the component molecules in the vdW precursor, liberating a "hot" atom that attacks the nearby coreagent). A second ultrashort, suitably tuned, variably delayed probe laser pulse detects either the intermediate complex or the newly born product. From an analysis of this temporal data as a function of pump and probe wavelengths, the real-time dynamics of such a "van der Waals-impacted bimolecular (VIB)" reaction can be determined. Chosen as a demonstration example is the VIB reaction H + CO$_2 \rightarrow$ HOCO$^{\ddagger} \rightarrow$ HO + CO, using the HI·CO$_2$ vdW precursor. The pump laser wavelength was varied over the range 231–263 nm; the probe laser detected OH in two different quantum states. The measured rates of formation and decay of the HOCO‡ complex are characterized by time constants τ_1 and τ_2; τ_2 spanned the range 0.4–4.7 ps, varying with the available energy. The dynamics of the HOCO‡ decay are discussed.

I. INTRODUCTION

Real-time probing of chemical reactions with ultrafast laser pulses allows one to observe the act of bond breaking and bond formation in unimolecular (half-collision) and bimolecular (full-collision) processes.[1] Since the duration of the pulses can be as short as tens of femtoseconds, subangstrom resolution of the interfragment motions can now be attained. For unimolecular reactions, the *zero-of-time* is very well defined by the pump laser pulse, and one can precisely monitor (with the delayed probe laser pulses) the temporal evolution of the transition states and nascent fragments.

For bimolecular reactions, however, the situation is different. To follow the dynamics of bimolecular reactions in real-time, one encounters a conceptual problem. Here, unlike the unimolecular case, "clocking" cannot be done, since there is no comparable way to establish the "beginning point", i.e., the *zero-of-time*, for the reaction. Even if one attempted to initiate the reaction by using a short laser pulse to form, say, radicals that can then react, the radicals would have to first find each other and collide before reaction could possibly occur. In the dilute gas phase, these transit times are typically in the nanosecond to microsecond range, many orders of magnitude longer than the femtosecond-to-picosecond times needed to traverse the transition-state region.

It is now established[2] that there are two broad classes of bimolecular reactions, depending on the lifetime of the collision complex. "Direct-mode" chemical reactions are characterized by subpicosecond reagent interaction times; "complex-mode" reactions are those involving "long-lived" (i.e.,

several rotational periods) collision complexes. It is this time scale, characteristic of the collision complex, which determines the fate of the products.

Traditionally, bimolecular reaction dynamics have been studied by the crossed molecular beam scattering technique.[3] From the anisotropy of the products' angular distribution (PAD) in the center-of-mass coordinate system, it is possible to infer certain important dynamical features of the reaction. In this regard, quasiclassical trajectory calculations[4] on *ab initio* (or even semiempirical) potential surfaces[5] and statistical theories of formation and decay of collision complexes[6] have been instructive. More recently, spectroscopic methods have been utilized for product state analysis, and a wealth of detailed experimental results are now available. In these experiments, the main body of information has come from post-collision observables, i.e., product state distributions (PSDs) via chemiluminescence[7] and laser-induced fluorescence (LIF),[8] PADS,[9] and products' alignment.[10]

In an earlier communication,[11] we reported on a direct experimental method for real-time probing of bimolecular reactions. We established the *zero-of-time* by using an ultrashort laser pulse that initiates the reaction via the photodissociation of a van der Waals (vdW) precursor molecule. We term this a "van der Waals-impacted" bimolecular (VIB) reaction.

The method is illustrated by way of the reaction of H with CO$_2$. The starting coreagents were implicit in the van der Waals molecule, HI·CO$_2$, prepared in a seeded supersonic jet expansion. The pump laser pulse photodissociates the HI in the vdW precursor coreagents, and the resulting translationally "hot" H atom initiates the bimolecular reaction. The clocking of the reaction is then accomplished by the use of a probe laser pulse which is delayed in time with respect to the initiation pulse, and which is tuned into reso-

[a] Present address: Department of Chemistry, University of Chicago, 5735 South Ellis Avenue, Chicago, IL 60637.
[b] Sherman Fairchild Distinguished Scholar at Caltech. Permanent address: Department of Chemistry and Biochemistry, University of California, Los Angeles, CA 90024.

nance to monitor the time development of the OH reaction product.

Use of such a "precursor-geometry limited" method to study product state distributions of bimolecular reactions has been pioneered by the groups of Jouvet and Soep[12] and Witting and coworkers[13] As discussed below, these constrained systems are unique in "defining" a limited range of impact parameters and orientations for the subsequent bimolecular encounter. However, the intermolecular vibrational mode has a large amplitude, and this may cause the range to be quite large.

In this paper we provide details of the concept of the real-time pump-probe technique and the experimental methodology. We present a full account of our earlier work,[11] focusing on the application of the method to the H + CO_2 reaction, involving the intermediate HOCO. We discuss the analysis of the temporal data (i.e., the OH formation) obtained at different total energies (governed by the pump laser wavelength). The results are then interpreted in terms of the reaction dynamics, and discussed in relation to recent experimental (PSD)[14] and theoretical studies.[15]

II. TECHNIQUE

Figure 1 illustrates the concept of the experiment. The coreagents (e.g., HI and CO_2) are jet expanded with a carrier gas (e.g., He) to form a cold molecular beam of HI·CO_2.
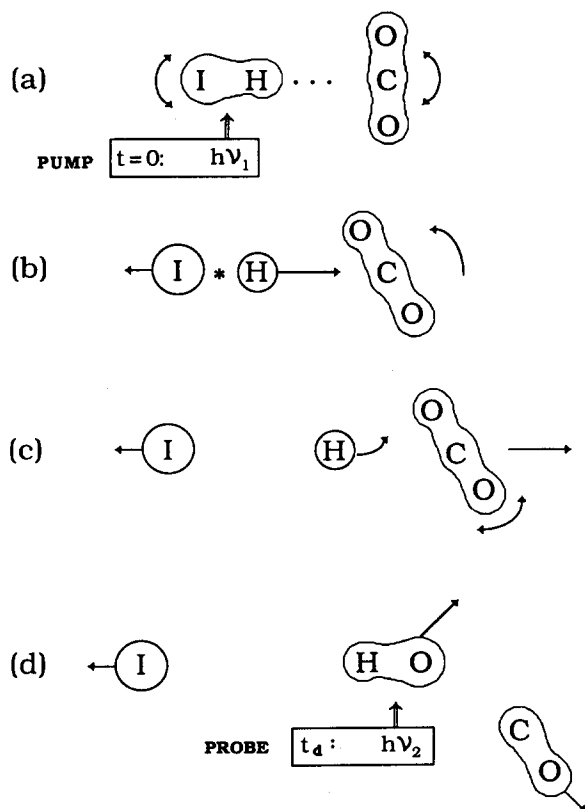

FIG. 1. Concept of the experiment. (a) Zero-of-time ($t = 0$) established by pump laser pulse (λ_1), photon energy $h\nu_1$, which photodissociates the HI component of the HI·CO_2 vdW molecule. (b) The translationally hot H atom is ejected toward its CO_2 "partner." (c) The H atom forms the HOCO complex, which then undergoes intramolecular vibrations, falling apart to yield (d) OH (and CO), detected at a time t_d by the probe laser pulse (λ_2) photon energy $h\nu_2$.

The vdW molecules are identified and characterized by electron impact time-of-flight mass spectrometry (EI-TOFMS). Two ultrashort laser pulses are utilized in the clocking. The first (photolysis) pulse establishes the *zero-of-time* by producing a hot hydrogen atom in the vdW species (in the generic sense, X-H$\cdots ABC$). Since the H atom is produced with high velocities, typically 20 km s^{-1}, a motion of 2 Å towards ABC will require only ~ 10 fs. The formation of a collision complex ($HABC^\ddagger$) in such short times would be resolved in real time if the second (probe laser) pulse wavelength were tuned to an absorption of $HABC^\ddagger$, and the pulse's time resolution were better than 10 fs. Successive probe pulses delayed by increasing intervals would then yield a rise (with time constant τ_1).

If, instead, the second (probe) pulse monitors the *final fragment* (say HA) from the decay of the $HABC$ complex, then the time evolution of the probe signals will reflect the *dissociation of the collision complex*. For complex-mode[16] reactions the $HABC^\ddagger$ is expected to decay, relatively slowly with time constant τ_2, to the final fragments. Thus, measurement of τ_1 and τ_2 characterizes the type of reaction and the nature of the collision complex, formed with a given total energy (governed by the pump laser wavelength).

For "direct-mode" reactions, τ_2 will be much shorter than in the case of complex-mode reactions, and will typically be less than a picosecond. In this limit of a very short-lived complex, the present technique is also applicable, but femtosecond pump and probe laser pulses are required.

Real-time probing of the reaction and clocking of fragments from the *zero-of-time* is accomplished by delaying the second probe pulse relative to the initiation pulse using a scanning Michelson interferometer, before both pulses are directed to the laser-molecular beam intersection zone. A "distance delay" of 3 μm corresponds to a temporal delay of 10 fs. Naturally, it is essential to characterize the pulses via autocorrelation and cross-correlation methods, since the determination of the exact *zero-of-time* is of the utmost importance. At present these attributes can be measured with femtosecond precision. Thus, with femtosecond transition-state spectroscopy (FTS) techniques[1,17] detection of transition states for this class of reactions can be made.

There are a number of points about this approach to bimolecular reaction dynamics that should be discussed. First, the fact that the reagents are in close proximity at times prior to the reaction zero-of-time means that there is a limited range of impact parameters dictated by the vdW forces (i.e., the structure of the vdW precursor molecule). This feature helps one to unravel the dynamics for a "specified" initial geometry, and in fact, by varying the X atom in the HX one could vary this geometry. The dynamics might well be different from the bulk gas case in which there is averaging over all approaches and impact parameters.[3] The presence of X may also change the available energy (i.e., X may not simply be a "spectator"). This can be explored experimentally by varying X, and by replacing H by D. Nevertheless there are great advantages in studying (in real time) such VIB reactions.

Second, the analysis given above invoked a classical kinetic description of the formation and decay of the collision

complex. A quantum mechanical analog can be made, as in other cases like IVR[18] and predissociation dynamics.[19] Basically, if the phase space of the vibrational/rotational motion is large enough, the initial wavepacket can be described "statistically"; following the initial dephasing one achieves equilibration. This picture can be approximated by a kinetic treatment,[20] where one decay process corresponds to the dephasing and another accounts for the lifetimes of the eigenstates. In the absence of coherence effects this analogy can be made and has been used in several applications, keeping in mind the known limitations. (For example, the kinetic approach is not able to handle vibrational quantum beats.)[18] It is not necessary to use this kinetic equation approach; quantum calculations could be compared directly with experimental results, as has been done in other FTS studies[17,21] of unimolecular reactions.

Third, in addition to the above reaction clocking measurement, one can study the vector properties of the VIB reaction. As pointed out elsewhere,[22] and shown experimentally,[23] the use of polarized laser pulses (both pump and probe) provides a means for measuring the time dependence of the product alignment. From such measurements one can obtain the alignment coherence time, which is governed by the torque that leads to fragments' rotations. For the VIB reactions, this type of measurement would establish in a direct way the average "rotation time" of the collision complex, τ_r.[22] If both τ_r and τ_2 have been measured, one could directly characterize the mode of the reaction $\tau_r \ll \tau_2$ (complex mode) or $\tau_r \gg \tau_2$ (direct mode). Finally, probing the separate final rotational states of the product could provide information on the change in the "mode" (complex versus direct) of the reaction as a function of the rotational state of the complex.

III. EXPERIMENTAL

Here we outline the general laser/molecular beam system used in these studies. For the particular application in this paper, namely, the VIB reaction of $H + CO_2$, we give details regarding the laser system, the molecular beam system, and the diagnostic experiments. The experimental design was implemented with several objectives and constraints in mind. The objectives include (1) attaining the ability to measure directly the real-time dependence of the concentration of the OH product, (2) simultaneously maintaining sufficient temporal resolution and the capability of spectrally resolving the $(^2\Sigma \leftarrow {}^2\Pi)$ electronic transitions for OH formed in a single specific rotational state, (3) measuring the temporal response function of the laser system in such a way that the zero-of-time of the reaction is obtained with maximum accuracy, (4) developing a continuously tunable excitation (pump) laser light source which could be scanned over a large wavelength range, thus facilitating study of the energy dependence of the reaction dynamics, and (5) having sufficient control of the reactant gases and providing *in situ* diagnostics of the molecular composition of the free-jet expansion.

Attainment of the first two desired objectives is, of course, restricted by the Heisenberg uncertainty relation

$\Delta\tau \cdot \Delta v = 0.44$ (for a Gaussian pulse envelope). The spectral resolution necessary to satisfy the second objective is dictated by the spacing of the aforementioned OH electronic transitions of adjacent values of the rotational quantum number for the ground-state product. Isolating Q-branch transitions, one calculates an upper limit frequency bandwidth of ~ 10 cm^{-1}.[24] In the case of a Gaussian pulse shape, this means pulse durations of full width at half maximum (FWHM) $\geqslant 1$ ps. The experimental results reported herein were obtained with an amplified synchronously pumped dye laser system. The dye laser/amplifier scheme which was employed allowed for obtaining near-optimal frequency and temporal conditions. This was facilitated by essentially continuous control of the laser spectral bandwidth and by minimizing gain saturation in the amplification.

A. Pulse formation, amplification, and continuum generation

The essentials of this laser oscillator and amplifier apparatus have been previously described,[25] and the pulse generation and amplification arrangement is shown in Fig. 2. The output of an actively mode-locked Nd:YAG laser was frequency doubled to produce an 82 MHz output of 10 nJ, 80 ps, 532 nm pulses. These pulses synchronously pump a cavity length-matched (within 1–3 μm) dye laser. The dye medium was a mixture of R6G dye and DQOCI saturable absorber. The dye laser gave pulse autocorrelations of 3 ps FWHM, as measured by a home-built, spinning block autocorrelator. A two-plate birefringent filter was used as the cavity tuning element. The dye laser was run in a fashion which restricted the minimum temporal pulse duration by the spectral bandwidth limiting element while also obtaining favorable conditions for good mode locking via rapid quenching of the gain by the saturable absorber. These oscillator pulses were monitored on a continuous basis with the spinning block autocorrelator.

The principal fraction of the dye laser beam intensity was injected into a four-stage pulsed dye amplifier pumped by a 20 Hz, 300 mJ Q-switched YAG laser. The first two stages were optically separated by either a 25-μm-diam diamond-pinhole spatial filter or a 200-μm-thick dye jet of 5×10^{-4} M malachite green (MG) in ethylene glycol. The second and third stages were separated by a 50-μm-diam diamond-pinhole spatial filter. The spatial filter acts to reduce the amount of amplified spontaneous emission (ASE) intrinsic to the present pulsed dye-amplifier design. The first three stages were transversely pumped with increasing fractional amounts of the 532 nm Q-switched YAG output. The fourth stage was longitudinally pumped by the remaining 50% of the 532 nm beam. The picosecond beam diameter was matched to the size of the YAG transverse beam diameter. The input pulse energy was increased from 0.5 nJ to 0.3 mJ, for a gain of nearly 10^6.

The MG dye absorber jet was employed in most of the experimental measurements. The saturable absorber reduced the amount of pulse width broadening to less than 50%; even less pulse width broadening could be obtained for lower amplification gain factors. The absorber jet was also somewhat more effective than the spatial filter in reducing
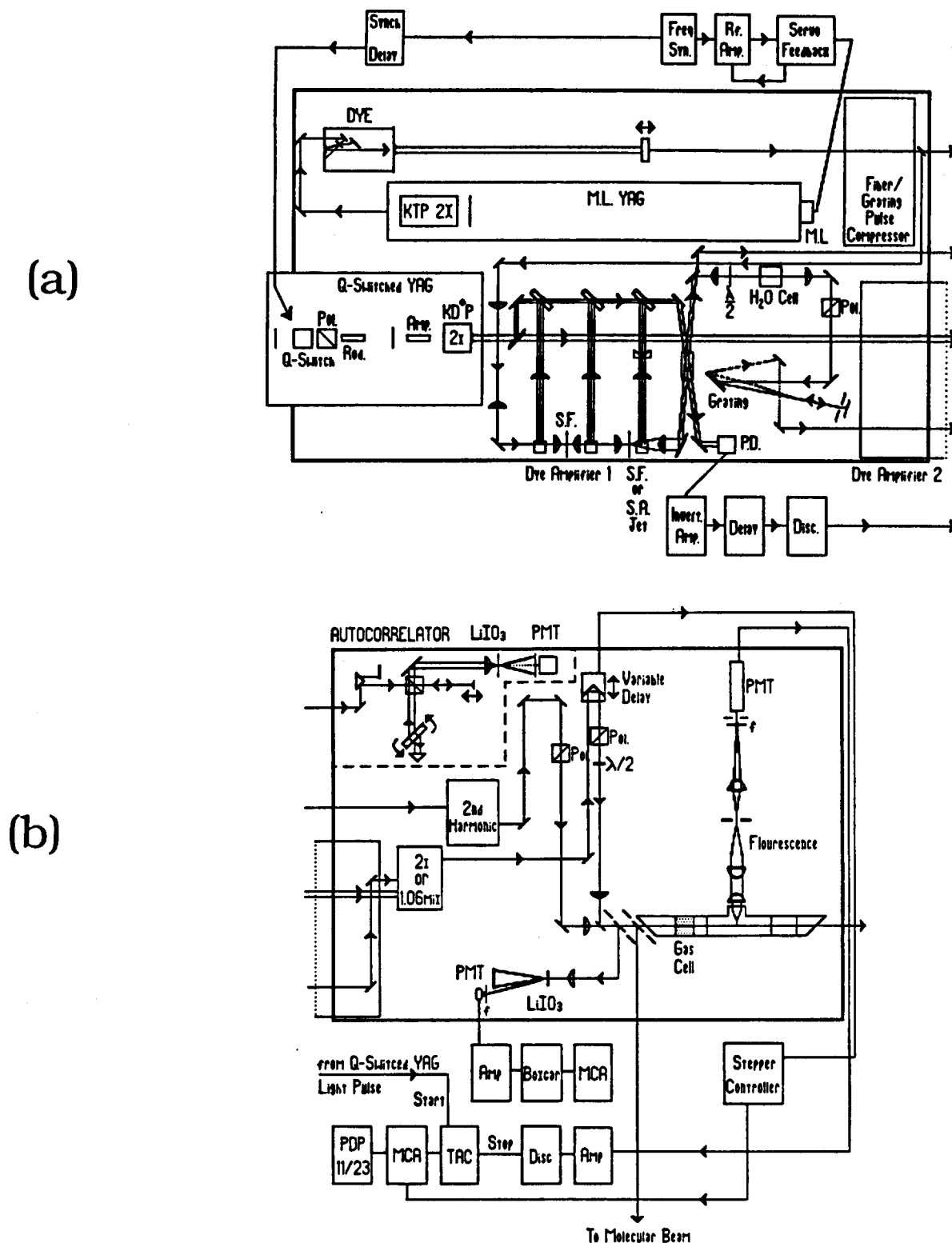
FIG. 2. (a) The laser oscillators and pulsed dye amplifiers are shown. The path of the light beams is indicated. The position of the continuum generation optical arrangement is also indicated. (Further details in text.) (b) A schematic diagram of the second experimental setup, which contains the scanning delay line interferometer, nonlinear frequency-generation optical arrangement, the spinning block auto-correlator, and the low scattered-light gas sample cell. (See text.)

the ASE which originates in the first stage. The dye in the amplifier stages was a mixture of R640/CV670 in a ratio of about 10–15:1. The solvent was methanol in all stages, the concentration of the dye being about 2×10^{-4} M in the first

two stages and 5×10^{-5} M in the last two. The dye mixture was used in an energy transfer mode to obtain enhanced gain near 619 nm when the $Q_1(6)$ transition of the OH was probed.

The amplified picosecond beam is split by an 80% reflectance beamsplitter; the transmitted 20% of the beam is frequency doubled and used as the probe beam. The majority of the light is focused into a cell of "nanopure" (i.e., filtered and de-ionized) water and results in the creation of an optical continuum.[26] (Such an optical continuum is obtained when a sufficiently intense optical field interacts with the third-order nonlinear susceptibility of the medium.) The spectral continuum is produced to allow for good pump-probe laser pulse synchronization with a minimum of relative timing jitter. The continuous frequency light source is to be used as the seed light pulse for a second amplifier.

The white light continuum is obtained in the following fashion. A half-wave plate rotates the plane of polarization of the light source entrant on the continuum cell to the horizontal. The horizontal polarization enhances the reflection or transmission efficiency of the optics which are to follow.

An 8 cm fl lens focuses the beam into a 2-cm-long cell of water. The continuum beam is recollimated with a 6 cm fl achromat lens and is analyzed with a polarizer, which is set to transmit only horizontally polarized light. Self-phase modulation (SPM), observed to be a significant (and the presently desired) mechanism in continuum generation,[27] should maintain the same polarization of light as the entrant beam. Extensive optical manipulation of this light source is required for spectral bandpass selection, limited pulse shaping, and finally amplification to the 0.1–0.25 mJ level. (See Fig. 3).

Following the polarizer, the beam is diffracted by an 1800 lines/mm ruled diffraction grating and is directed into a cylindrical lens (15 cm fl) placed 20 cm after the grating face. A variable aperture slit is positioned at the focal plane of the cylindrical lens. A normal incidence mirror, located immediately after the slit, retroreflects the spectrally select-
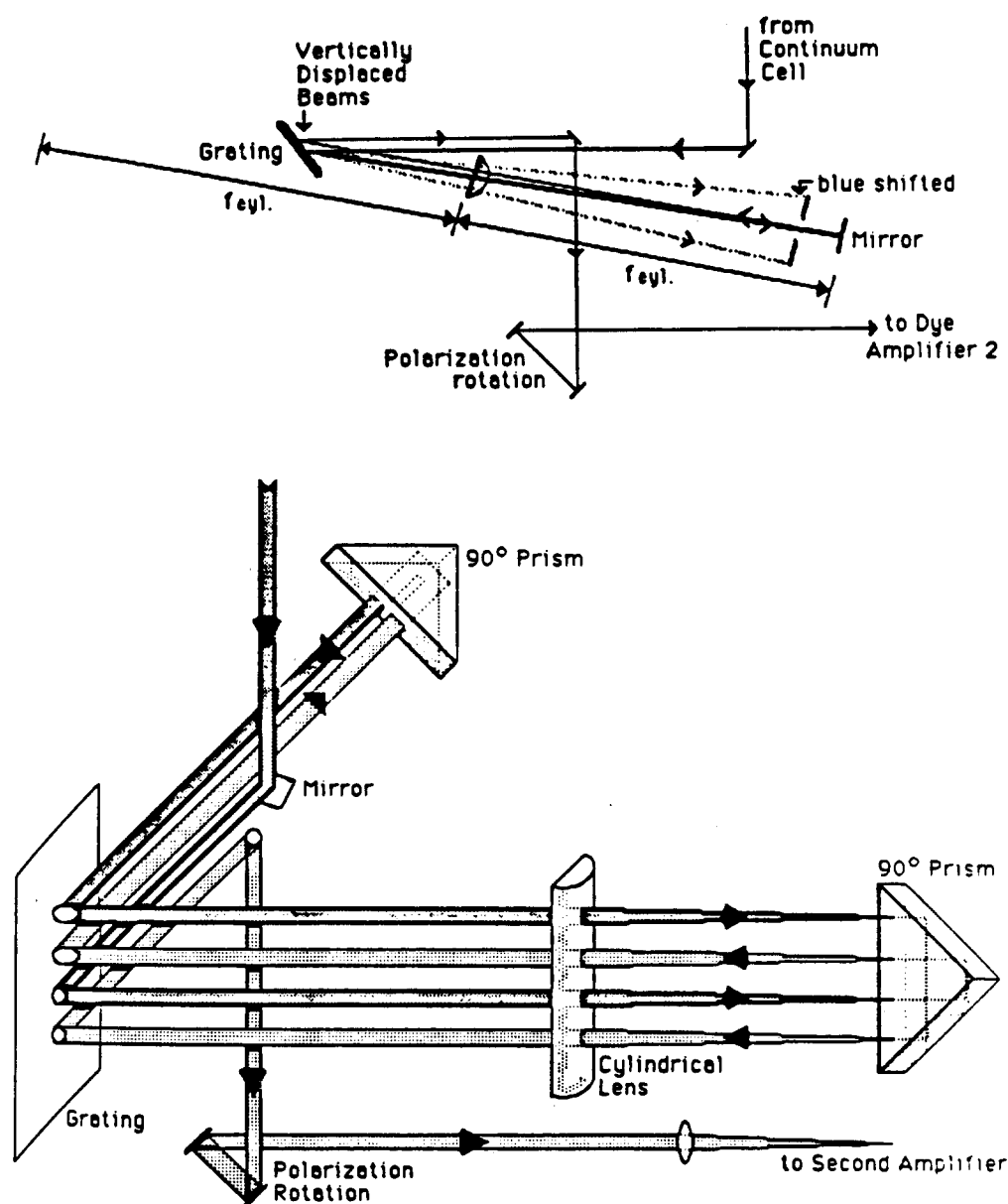

FIG. 3. (Upper) Schematic drawing of the double-pass diffraction grating/cylindrical lens and slit arrangement that allows for spectral selection of a frequency bandpass from the optical continuum. The separation of the lens and grating relative to the focal length of the lens may be adjusted to alter the sign and magnitude of the linear chirp imparted on the spectrally selected pulse. (Lower) A quadruple-pass optical arrangement that serves the same function as the above. The added feature of this design, obtained at the expense of throughput efficiency, is to remove the transverse-mode frequency sweep.

ed beam back onto the grating but displaced ~2 cm below the level of the entrant beam. The resultant spectrally selected pulse, with a 3 Å FWHM bandwidth, has approximately the same temporal duration as the pulse exiting the first amplifier. The pulse energy of this spectrally selected portion of the continuum varies from about 25 nJ near the center frequency to less than 0.5 nJ at 470 nm. These pulse energies are sufficient to be injected into and serve as a seed for a second dye amplifier, pumped with either the second or third harmonic of the Q-switched YAG laser. The three-stage amplifier, with the last stage being longitudinally pumped, could produce amplification factors in the range $\sim 2 \times 10^4 - 5 \times 10^5$ depending on the pump wavelength, amplifier dye, and initial spectrally selected continuum picosecond pulse energy.

It has been shown[28] that the introduction of a lens of focal length longer than its separation from the grating face will allow for the introduction of positive group velocity dispersion (GVD) on the exiting beam, causing a positive linear chirp to be introduced in the pulse temporal behavior. It is also known[29] that a grating pair arrangement introduces negative GVD. This latter arrangement has been applied to pulse recompression following dispersion in optical fibers. The present arrangement introduces negative GVD and acts to compensate for ~0.5 ps of pulse broadening. Such temporal dispersion arises from the dispersion of the index of refraction in the glass lenses, suprasil dye cells, and the dye medium of the amplifier. In particular this negative GVD acts to offset some of the positive GVD introduced by the second amplifier.

B. Pump-probe scheme

The time-resolved experimental studies have been performed over the wavelength range 231–263 nm. It is possible to amplify 474–530 nm light using the 355 nm YAG pump and several dyes (coumarins: 522, 500, 481, 480, 460; Exciton Chemicals) in polar and nonpolar solvents (ethanol, hexane, cyclohexane). Second-harmonic generation of the amplified continuum light allowed for essentially continuous coverage of the wavelengths 237–265 nm. The frequency doubling is performed using a 4 mm (thickness) β-barium borate (β-BBO; CSK Co.) crystal placed slightly after the beam waist of a 1 m focal length lens. This second-harmonic light is used as the experimental pump beam and served to initiate the reaction. The higher energy portion of the wavelength range (230–238 nm) is reached with pump light obtained by doubling the 587–613 nm output from the second amplifier (in a KDP crystal) and mixing this doubled light with the 1.064 μm fundamental of the YAG laser (in a type II KD *P crystal). The various frequencies are dispersed using a Pellin–Broca prism. As before, the 20% remainder of the beam from the first amplifier is used to form the probe beam.

A schematic outline of the experimental arrangement is shown in Fig. 2(b). The visible pulse propagates through a variable delay line stepper motor/worm gear translation stage (10 μm/step resolution) to obtain the timing delay between the pump and probe pulses. The beam is then focused ($f = 40$ cm) into a 1 mm KDP crystal, recollimated with a 20 cm suprasil lens, and sent toward the molecular

beam apparatus. A waveplate ($\lambda/2$) is used to adjust the relative pump–probe polarizations. Focusing into the thin nonlinear crystal, and in particular placing the crystal within a confocal length of the position of the beam waist, causes the second-harmonic beam transverse profile to become much less structured than the entrant fundamental beam.

The pump and probe beams are independently focused, through a quartz window, into the molecular beam apparatus as seen in Fig. 4. A 150 μm diamond pinhole inside the chamber and on the axis defined by the molecular jet orifice and the skimmer, but positioned perpendicular to the direction of the jet expansion, is used to overlap the pump and probe light beams. A 0.75 m planoconvex (plcx) lens is used to focus the pump beam, and a 1 m plcx lens focuses the probe light. The pump and probe beams are combined by a dichroic reflector (coated to allow for 80–90% transmission of the probe light) and propagate collinearly through the molecular beam apparatus. This arrangement allows the beam waists of the pump and probe light to be independently adjusted and matched to the axis of the free-jet expansion (i.e., the molecular beam axis). Both laser beams show significant diffraction from the 150 μm pinhole, with the probe beam being somewhat larger in diameter. The pump pulse energy is 5–10 μJ (25 cm^{-1} FWHM bandwidth), and the probe pulse energy is attenuated to be <1 μJ with a 6 cm^{-1} FWHM Gaussian spectral width.

C. Molecular beam and sample characterization

The pulsed nozzle of the molecular beam apparatus is operated by a circuit to provide an electrical pulse to the valve in synchrony with the Q-switched laser firing. The
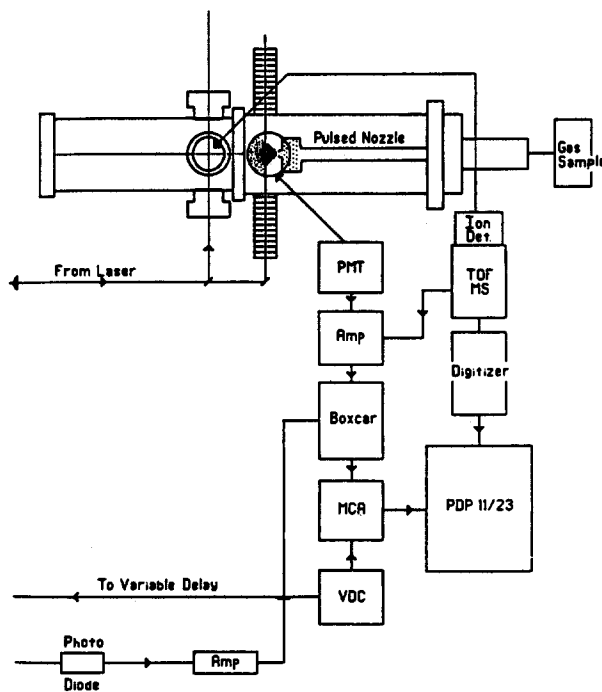

FIG. 4. Schematic diagram of the experimental arrangement, including the detection instrumentation for the LIF and TOFMS signals originating from the respective crossed laser-molecular beam regions within the experimental chamber. (See the text for details.)

vacuum chamber is constructed of two cylindrical chambers separated by a 1.7 mm opening tapered-cone Ni electroformed skimmer. The skimmer allows for differential pumping of the two chambers, with nominal pressures of 2×10^{-4} and 4×10^{-6} Torr obtained in the primary and secondary chambers, respectively. Each volume is pumped with a 6 in. diffusion pump and is isolated from the pump via LN_2 cryobaffles. The baffles effectively eliminate backstreaming of pump oil. The primary chamber, which handles $> 95\%$ of the gas load, is arranged with the nozzle, laser entrance and exit (light baffle) ports, and the LIF collection optics (and the $150 \mu m$ pinhole) on three mutually orthogonal axes. The second chamber also has three such mutually orthogonal axes, one defined by the now-skimmed molecular beam, the second containing entrance and exit optical ports for the laser light (not used in this study), and the third consisting of the electron impact time of flight mass spectrometer (EI-TOFMS), described below.

The nozzle assembly in the primary chamber is of Kel-F and Teflon coated metal construction. The generic valve design has been described before.[30] Briefly, it is a solenoid-plunger design, wherein a current pulse energizes the solenoid coil, which, in turn, retracts a metal piston. The piston pulls a Viton-tipped Vespel plunger to expose the orifice opening. The valve is closed by the action of a small spring which forces the Vespel/Viton plunger to seal the opening. All of the exposed metal surfaces have been coated with a thin film of Teflon to prevent the catalytic decomposition of the HI in the nozzle plenum just prior to the expansion. The orifice is a 1.6-mm-thick stainless-steel disk (held to the Kel-F nozzle body by a screw-on cap) with a 500-μm-diam hole. The screw cap contains a 45° conical aperture, 2 mm long, centered on the orifice position. This conical extension acts to enhance the cooling and thus the dimer-forming efficiency during the early collisional portion of the expansion.

The nozzle open time is controlled by the magnitude (voltage) and temporal duration of the electrical pulse to the solenoid (120V, 550–600 μs). The resultant open time, as measured by the EI-TOFMS, was in the range 600–800 μs. The time-delay between the firing of the electric pulse (opening the valve) and the laser firing is adjusted to optimize the concentration of the desired vdW molecule at the time of arrival of the laser pulses. The pulsed nozzle controller is triggered by a monitor pulse from the Q-switched YAG which comes 3.3 ms prior to laser Q-switching. The controller is adjusted to generate an appropriate internal timing delay. The adjustment is made by optimizing the $1 + 1$ molecular complex ($HI \cdot CO_2$ parent ion) signal observed by EI-TOFMS. The repetition rate of the pulsed valve was that of the pump-probe laser pulses.

The traditional problem of identification of the 1:1 neutral complex with the 1:1 ion detected mass spectrometrically and the question of "evaporation" common to cluster ions occurring during the drift period was partially addressed by monitoring the ion peak intensities in rich HI-CO_2 mixtures. The relative parent peak intensities of the 1:1, 1:2, and 2:1 complexes were recorded for electron impact energies varying from 20 to 70 eV. It was found that these relative peak intensities did not change up to 40 eV. That is, fragmentation

of the ions $(HI)_2 \cdot CO_2$ or $HI(CO_2)_2$ does not produce detectable levels of the 1:1 ($HI \cdot CO_2$ parent ion) signal, provided sufficiently low electron impact energies are used. This is consistent with reported observations for $HF \cdot CO_2$.[31]

D. Gas mixture and beam characterization

A sample handling and dynamic flow gas mixing apparatus was constructed to allow for flexibility and efficiency in the adjustment of the relative concentrations of the constituent gases. The nozzle expansions are performed with helium as a carrier gas; He was chosen since the propensity to form larger aggregate complexes with this carrier is diminished. High-purity He and CO_2 are premixed to a 4% concentration of CO_2. The exact concentration is adjusted to allow for the slight ($\leqslant 5\%$) dimerization of CO_2 in the He-CO_2 expansion at the operational nozzle conditions (total pressures in the range 2–3 bar). The HI (Matheson) was purified just prior to and during use by cold trapping (retaining the disproportionated I_2). The HI and He-CO_2 gas flows passed through separate flowmeters (Matheson rotameters) and were combined just after the meters. The nozzle expansion pressure (1700–2100 Torr) was adjusted primarily with the He + CO_2 flow. The HI-regulated pressure is greater on the inlet side of the associated flow meter. A microadjustable needle valve allows for dynamic adjustment of the HI concentration in the mixture. The positive pressure across the valve allows for continuous and steady HI flow. This type of a flow scheme relies on stable pressures of the constituent gases; adequate stability is maintained with a two-state regulator on the He + CO_2 tank and a two-stage corrosive gas regulator on the HI lecture bottle. The dynamic mixing requires flow rates of 50–100 Torr ℓ min^{-1} to facilitate ease of adjustment. The entire entrained gas flow passes through a final 15 °C (glycol-dry ice) trap just before entering the nozzle plenum. All subsequent surfaces contacted by the gas mixture are constructed of inert plastic materials.

The initial composition of the gas flow is only coarsely adjusted with the flow meters. The final composition is set by adjustments made while monitoring via the EI mass spectrum, noting relative signals of HI-CO_2^+ versus HI-$(CO_2)_2^+$ and $(HI)_2$-CO_2^+ ions from vdW complexes. The ratio of the desired 1:1 complex to the higher clusters was always optimized to exceed 10:1. This required adjusting the HI composition to 1.5% of the total as monitored by the rotameters and in EI-TOFMS. (See Fig. 5.)

The EI-TOFMS arrangement consists of a pulsed electron gun juxtaposed with several voltage grids, a TOF field-free drift region (1 m length), a grounding grid, and a box and grid design ion detector. The electron gun consists[32] of a W filament in a Faraday cup and an extraction (gate) grid. A dc power supply provides 3.5–4.0 A of current to the coiled W wire (0.005 in. diameter) filament. The Faraday cup is held at the potential of the low side of the filament, which (along with the covering extraction grid) serves to "store" the electrons. The gate grid is held several volts below the filament potential and is pulsed 20–30 V above the filament potential for about 1 μs to extract the electrons.

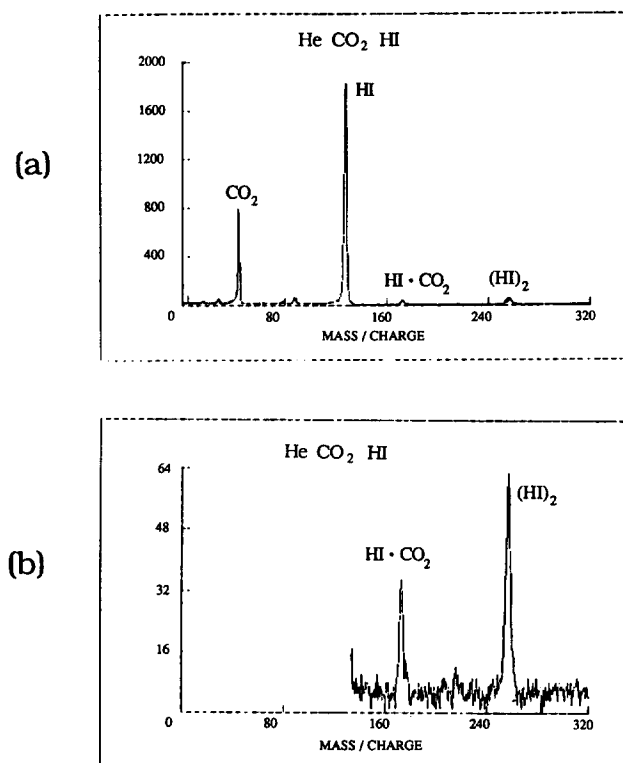The repeller, accelerator, and ground grids are located

FIG. 5. (a) EI-TOF mass spectrum for a supersonic jet expansion of a He:CO_2:HI mixture. The relative compositions were 95.5:4:1.5; stagnation pressure ~1800 Torr. The deflection plate voltage has been adjusted to optimize the detection sensitivity in the 120–200 amu range. This tends to discriminate against the lower mass species, especially He and CO_2. Electron impact energy 30 eV, repeller voltage 440 V, accelerator 400 V, and filament biased at 370 V. (b) Expanded portion of the mass spectrum showing HI·CO_2 and (HI)$_2$ peaks.

directly above the electron gun, and all of the grid spacings are about 3 cm. The grid voltages have been chosen in accord with considerations of first-order space focusing.[33] The grounding grid is followed by two parallel, vertically oriented electrodes which, when properly biased, act to deflect the ions of a given m/z range toward the detector. A second grounded grid, located 1 m above the first, defines the end of the field-free region of the TOF drift tube. The ion detector cathode, at − 3000 V, located beyond the grounding grid accelerates the ions to energies sufficient to initiate the electron cascade through the ion-electron multiplier (18 dynode) detector.

The 50 Ω terminated output of the multiplier is fed into a 500 MHz wide band ×10 amplifier (PAR model 115). Its output is fed to a boxcar integrator/averager unit (PAR model 164, 162 averager), which produces an output voltage proportional to the current monitored in the 50 ns integrator gate width. The voltage output is fed to a voltage-to-frequency converter (VFC), and the signal is stored in a multichannel analyzer (MCA, Tracor Northern). The time delay position of the boxcar gate may be swept in time to perform the scan of a mass spectrum. Alternatively, the output of the ×10 amplifier is fed into a transient digitizer (LeCroy) which serves to simultaneously sample 1000 sequential 40–80 ns time intervals and digitize the analog voltage signal of

the entire mass spectrum (or a selected portion thereof) of every laser pulse. The parallel data collection system expedites the molecular beam diagnostics.

The mass resolution using either of the data acquisition methods described was ~4 amu at $m/z = 127$ amu. The mass resolution at the desired complex, $m/z = 172$, was about 6 amu. The mass spectral feature assigned to the desired complex is sometimes overlapped with the $(CO_2)_4^+$ ion (four mass units larger). This broadened double peak obtains for slightly too-rich CO_2 concentrations and results in two discernible peaks, at the 172 and 176 m/z positions.

A large dynamic range is inherently required to observe the CO_2 and HI signals, the 1:1 complex and the even weaker signals corresponding to the larger (undesired) clusters. The HI$^+$ ion signal level is about 100 mV, the CO_2^+ level 300–400 mV, and the He$^+$ peak saturates the detection/amplification system at a level in excess of 2 V. Figure 5 shows results of the EI-TOFMS scans for typical sample compositions.

E. LIF signal detection

The experimental signal is monitored by the LIF of the OH product, with the probe laser tuned to a specific transition within the $A\,^2\Sigma \leftarrow X\,^2\Pi$ electronic band.[24] The fluorescence is monitored at right angles to the laser and molecular beam axes. The laser, focused to a 150 μm beam waist diameter, intersects the molecular beam at $X/D = 40$–45, that is, 40–45 nozzle diameters downstream ($D = 0.5$ mm). The emission is collected by a 5-cm-diam 1-cm-thick suprasil window which forms the vacuum seal along this optical path. The collimated light next passes through a 12 nm FWHM interference filter (Andover) centered at 308 nm. Another plcx lens (f/1.5, 5 cm diameter) focuses the entrant light onto an adjustable slit, which is set to maximize the signal throughput and minimize scattered laser light. The necessity of detecting resonance fluorescence implies that it is not possible to discriminate against the light scattered from other portions of the chamber by spectral filtering. Instead of the interference filter, other filters may be placed between this f/1.5 lens and the slit, minimizing the amount of filter fluorescence reaching the detector. These were cutoff or bandpass filters Schott WG-320 and UG-11, respectively. Another f/1.5 lens recollimates the emission which passes through the slit, and a final f/1.5 lens, which is permanently mounted inside the PMT housing, focuses the emission onto the photocathode of a single photon counting PMT (Amperex XP2020). The PMT is mounted in a thermoelectrically cooled housing (Products for Research).

The 50 Ω terminated output is amplified by a wide band amplifier (PAR model 115, DC-500MHz) and sent to a constant-fraction differential discriminator. The discriminated pulse is fed to the "stop" input of a time-to-amplitude converter TAC (Canberra). The start pulse for the TAC is obtained from a fast photodiode (Hewlett–Packard), which monitors the Q-switched YAG laser pulse, and is amplified and inverted, then fed to a constant fraction discriminator (PAR). The TAC output is passed to the MCA, which accumulates the signal in synchrony with the stepper motor (delay line) advance. This single photon counting signal detec-

tion arrangement is also appropriate for time-correlated single photon counting detection. The MCA stores one count for every detected photon event. Since the channel position of the MCA is synchronized to the delay line step advance, the signal events are recorded for the appropriate pump-probe relative time delay. Typical accumulation times are 3 s per channel and the scans are repeated 15–20 times, depending upon the signal level and the enhancement over the background from the probe beam alone. The experimental signal level is, typically, about 1 count per second.

The gated detection (1 μs gate) obtained with the TAC and the low repetition rate of the laser amplifier reduces the dark count rate to less than 1 count in 10 s. The small-signal levels necessitate long experimental runs to obtain a sufficiently good S/N ratio to provide the desired accuracy in data analysis.

IV. ESTABLISHMENT OF THE ZERO-OF-TIME

A complete description of the time dependence of product (e.g., OH) formation for the reaction requires an accurate measurement of the "time-zero" and the correct system response function. Both are essential for the determination of the dynamical behavior. In previous FTS experiments,[1,17] Rosker *et al.* used a calibration method, developed by Scherer *et al.*,[34] to give an *in situ* response function and locate the time zero position. The idea was to use a "calibration molecule" introduced under identical conditions. With detection by multiphoton ionization (using the same pump and probe laser conditions), one establishes the position of the rising ion signal as a function of the delay time and obtains the zero of time for the reaction.

Here we have used another method to establish the time zero for the VIB H + CO$_2$ reaction. It consists of a one-photon (pump) photodissociation of HOOH and a one-photon (probe) LIF of the OH product at the same wavelengths as for the study of the HOCO system. The HOOH photolysis is performed with the identical optical alignment and delay conditions as those used for the VIB reaction, but in the molecular beam chamber at $P \simeq 50$–100 mTorr, $T \simeq 300$ K. The optical paths for the bimolecular experiment and the response function measurement are therefore identical. Moreover, the optimal pump-probe beam overlap is typically obtained using the bulb HOOH dissociation reaction. The optical alignment, once obtained and response measured, was not changed in proceeding to the VIB reaction study.

This scheme does not allow for monitoring the system response function simultaneously with the experiment and over the extended time interval of the OH signal collection. Also, although the HOOH response studies are performed under essentially collisionless conditions ($P \leq 100$ mTorr), the bimolecular reaction proceeds under free-jet expansion conditions into an ambient pressure of the order of $\sim 10^{-4}$ Torr. However, one can compensate for these deficiencies: for example, the HOOH response transient is obtained before and after each VIB reaction experiment. Any degradation of the system response function would therefore be detected. The signal obtained from the HOOH direct photodissociation and LIF detection is large enough to allow it to be integrated and averaged. The S/N ratio is about ten-

fold better than that of the VIB reaction data.

The HOOH dissociation and OH formation is sufficiently rapid to be termed "instantaneous" on the present experimental time scale (the dissociation of HOOH at these wavelengths takes place in <0.5 ps[34]). Figure 6(a) shows a comparison of the time dependence of the OH formation from the HOOH reaction with a true pump-probe pulse cross correlation obtained by difference frequency generation of the pump (256 nm) and probe [$Q_1(1)$] pulses in a 1 mm crystal of $KD*P$ with type II phase matching. [For comparison, Fig. 6(b) shows results obtained by the MPI method.] Figure 6 shows that the response may be convolved with a single exponential function with a lifetime of HOOH $\tau \leq 200$ fs which is indistinguishable from the difference frequency data. Such a short lifetime value is well within the intrinsic uncertainty due to the 4 ps (Gaussian) response
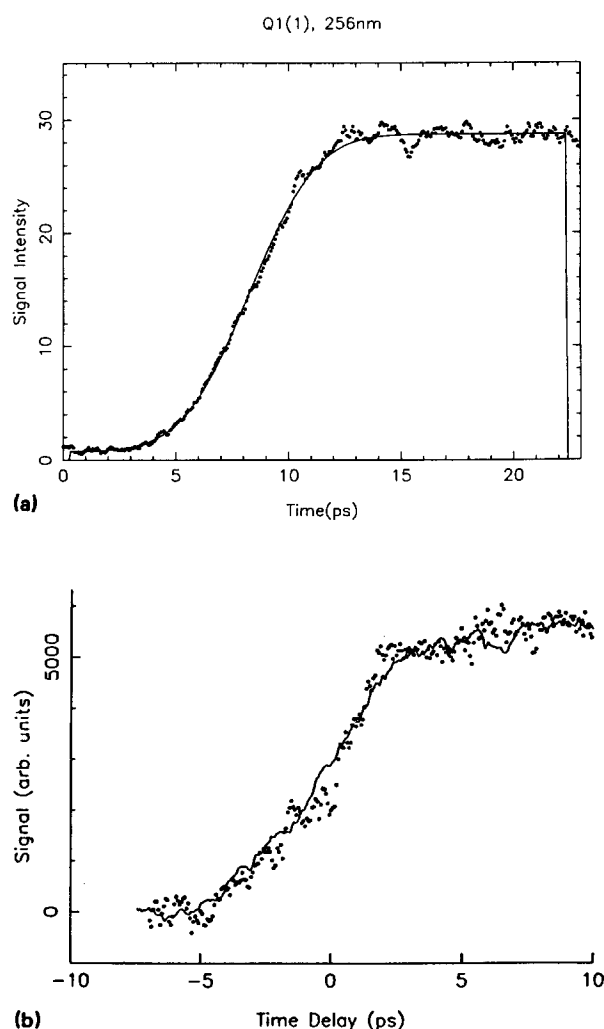

Q1(1), 256nm

(a)

(b)

FIG. 6. (a) Comparison of the observed transient, i.e., the time dependence of OH formation [via LIF at 308 nm, on the $Q_1(1)$ transition] from the photolysis of HOOH at 256 nm with a pump–probe cross-correlation obtained by difference frequency generation of the pump and probe pulses in a $KD*P$ crystal with type II phase matching. Circles denote experimental OH signals; solid curve, integrated fit with 5.5 ps FWHM Gaussian. (b) Comparison of *p-n*-butyl aniline MPI response function vs LIF of OH from HOOH direct dissociation (241 nm pump and 308 nm probe). The HOOH pump–probe LIF detection data are the circles; the ionization signal is the solid line. The data were obtained for parallel pump–probe polarizations.

which was obtained from the experimental pulse cross correlation. Care was taken to ensure that the pump and probe optical paths were equivalent in the HOOH and difference frequency studies. There was no detectable lag time between the inflection points of the two data sets.

The HOOH response method has been used to set the zero of time for the VIB reaction results presented in this paper for several reasons. First, as mentioned before, the HOOH photodissociation allowed for optimization of the pump and probe beam overlap under time delay conditions which are identical to those used in the VIB reaction. Second, since the signal from the HI·$CO_2 \rightarrow$ OH reaction is accumulated by photo counting at low laser repetition rates (20 Hz), it is much easier to maximize the obtainable signal with the *in situ* HOOH response. Third, the OH LIF signal from HOOH could be optimized for on-resonance $^2\Sigma \leftarrow ^2\Pi$ electronic transitions, facilitating probe wavelength tuning to the $Q_1(1)$ and $Q_1(6)$ transitions of the OH from the HOCO decay. Fourth, the HOOH dissociation may be used as a reference over the entire (~ 6000 cm^{-1}) pump laser wave number range used in this study. By contrast, several nonlinear crystals and IR detectors would be required to span the range of the difference frequency light.

Finally, the HOOH response method serves another useful purpose. The low count rates of the VIB reaction study preclude the possibility of measuring the power law dependence of the OH product. Since the detected photo product is the same for both reactions the power dependence is performed for the HOOH reaction. Figure 7 shows a logarithmic plot of the OH signal versus the decrease in the optical density, yielding a straight line with slope of 0.95 ± 0.1 for $Q_1(1)$ detection and 238 nm excitation, consistent with the view that a single probe photon induces the LIF of the OH product and the LIF intensity is proportional to the number density. A similar result was found when the $Q_1(6)$ transition was probed.

V. H+CO₂ VIB REACTION

A. Preliminaries and time-integrated experiments

1. Gas phase bimolecular reaction

The kinetics of the endothermic reaction H + CO_2 $\rightarrow$ OH + CO have been well studied, starting with the classic

experiments of Oldershaw and Porter[35] in 1969, followed by the work of Tomalesky and Sturm,[36] Quick and Tiee,[37] Wolfrum and coworkers,[38] and Wittig and coworkers.[13,14] Flynn and coworkers studied the inelastic scattering accompanying these hot-atom reactions.[39] It is a typical "hot-atom" reaction,[40] nowadays studied by the laser photolysis method in which a precursor molecule such as HBr or H_2S is photodissociated in the presence of CO_2, and the translationally hot H atoms initiate the reaction. The relative translational energy E_T for the bimolecular reaction is governed by the photon energy (i.e., the laser wavelength). The internal state distribution of the products (prior to collisional relaxation) are usually measured by LIF or MPI.

The kinetics of the reverse reaction have been studied by Smith and coworkers,[41] Golden and coworkers,[42] and Benson and coworkers.[43] Much of this work has been reviewed, e.g., by the Wittig group.[44] Scherer[45] has summarized the present status of the kinetics of the reaction (and its reverse). Wittig has discussed the energy dependence of the cross section and product state distributions,[44,46] so there is little reason for further review here.

Schatz, Harding, and coworkers[15] have carried out a number of theoretical (*ab initio* and semi-empirical) computations of relevant potential energy surfaces, as well as trajectory simulations thereon.

There is by now general agreement about the main features of the "microscopic mechanism" of the reaction, e.g., that it involves passage over a substantial (orientation-dependent) potential energy barrier, forming a relatively stable collision complex, namely HOCO‡, which can decay into CO and OH products. Figure 8 is a schematic representation of the reaction path.

Milligan and Jacox[47] have been able to characterize the HOCO species (both cis and trans isomers) by matrix isolation spectroscopy. Its lifetime as a collision complex is expected to depend upon its initial energy content when formed. Standard RRKM computations have been carried out by Wittig and coworkers,[13] by Sipes[48] and by Scherer[45] to estimate the lifetime of the HOCO as a function of the H + CO_2 collision energy E_T. Unfortunately, the uncertainty in the parameters used make it difficult to predict the lifetime with any degree of confidence. Furthermore, statis-
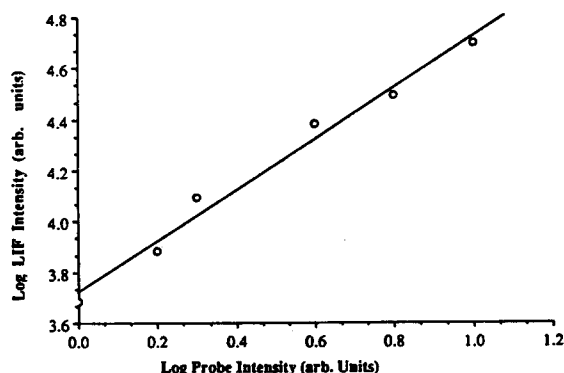

FIG. 7. Log–log plot of the OH LIF signal vs increasing probe beam attenuation for $Q_1(1)$ detection, 238 nm excitation. A best-fit straight line is shown (slope $= 0.95 \pm 0.1$).
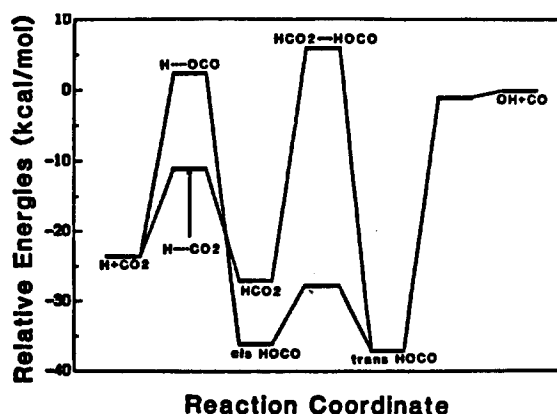

FIG. 8. Energy-level diagram that indicates the important barriers to reaction and minimum energies for the different configurations and transition state regions for HOCO (from Ref. 15). Energies in kcal mol^{-1}.

tical theories are not necessarily appropriate for such small systems, as discussed below.

Real-time measurements should help us address these points and critically examine theory versus experiments. Before summarizing the extensive new experimental results, related to the earlier work by Scherer et al.,[11] we shall first present some background information on the H + CO$_2$ VIB reaction.

2. *van der Waals precursor, i.e., VIB reaction*

Jouvet and Soep[12] first reported a photoinitiated bimolecular reaction in a vdW molecule (Hg...Cl$_2$) in 1983. Wittig and coworkers[13] extended this idea to the hot-atom reactions, specifically to that of HBr·CO$_2$. They photolyzed the HBr in the van der Waals molecule producing hot H atoms, and observed (by LIF) the internal state distribution of the resulting OH product. Indeed, they found a difference in the OH rotational state distribution relative to that from the analogous "bulk" gas phase hot-atom reaction, which could be attributed to the constrained initial geometry. They, as well as Jouvet, Soep, and coworkers have thoroughly discussed the advantages of this so-called "precursor geometry-limited" (PGL) photochemistry technique, wherein the range of impact parameters and initial mutual orientation of the reagents is severely restricted.

The Wittig group has since applied the method to the study of a number of hot H- and D-atom bimolecular reactions,[44] using LIF for the product state distribution measurements. The goal was to ascertain differences in PSDs due to the restricted initial geometry of the reagents in the vdW precursor molecules. For the H + CO$_2$ reaction from the fact that the PSDs for PGL reactions were usually "colder" than the bulk reactions, over a wide range of laser wavelengths and thus initial relative translational energies, they postulated that the internal energy of the HOCO complex was lower than that calculated from the nominal relative kinetic energy of the attacking H atom-CO$_2$ reagents (i.e., colder HOCO gives colder OH). Regardless of the details of the interpretation of the PSDs, the important conclusion is that the restrictive influence of the (equilibrium) geometry of the vdW precursor plays a significant role in the dynamics of the subsequent, bimolecular reaction.

In all of these experiments only the time-integrated (asymptotic) PSDs are the observables; no information is available on the *time evolution* of the products *per se*. Real-time data on the bimolecular reaction of H + CO$_2$ were first obtained by Scherer et al.,[11] using a picosecond laser pulse pump/probe technique to establish the *zero-of-time*, as discussed above, in this class of VIB reactions.

3. *Energetics*

For the bulk gas, hot-atom reaction in which the H comes from the photodissociation of HI, the average collision energy (relative translational energy in the center of mass H + CO$_2$ system) is given by[35]

$$\overline{E}_T = \left(\frac{m_1 m_{CO_2}}{m_{HI} m_{HCO_2}} \right) \times [E_p + \overline{E}_{int} (HI)$$

$$- D_0(HI) - E_{exc}(I)] \qquad (1)$$

Here the m's are the indicated masses, E_p is the energy of the pump laser photons, $E_p = hc/\lambda_1$, E_{int} (HI) is the average internal energy of the HI molecules in the bulb at some known temperature, $D_0(HI)$ is the bond dissociation energy of HI, and $E_{exc}(I)$ is the excitation energy of the I atom photofragment; zero for I($^2P_{3/2}$) and 7603 cm^{-1} (91.0 kJ mol^{-1}) for I*($^2P_{1/2}$). For the limiting case of a cold HI reagent ($E_{int} \simeq 0$), Eq. 1 can be written in practical form:

$$\overline{E}_T(kJ \, mol^{-1}) = 0.970(1.1963 \times 10^5/\lambda_1 - 294.7), \qquad (2)$$

for the ground state I channel. For the I* channel E_T is less by 88.2 kJ mol^{-1}. Figure 9 shows these relationships.

4. *Energetic and steric considerations*

In the ideal case, in which the halogen atom (X) is merely a "spectator" and plays no role following the photodissociation of the HX component of the vdW precursor, the available energy (E_{avl}) for the H + CO$_2$ reaction is the same as the E_T (c.m.) plus the internal energy of the CO$_2$ as calculated for the bulk gas reaction [Eq. (1)]. However, in the actual case, because the length of the hydrogen bond, although long, is not infinite, the interatomic potential between the X and the H atom is not yet zero when the latter is impacting the CO$_2$, i.e., the H atom has not attained its terminal, "free particle", hot-atom velocity. Thus the actual available energy of the HOCO collision complex may be lower than that calculated for the bulk gas case due to the energy transferred to the X atom.

This "energy deficit" for the HOCO‡ will reduce its decay rate. This will affect the theoretical interpretation of
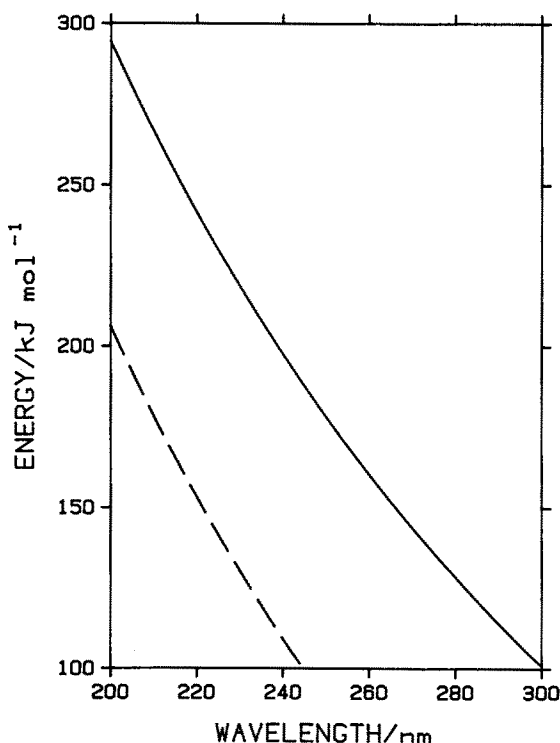

FIG. 9. Plot of Eq. (2) for the available energy (i.e., the total energy, in kJ mol^{-1}) as a function of the HI photolysis pump laser wavelength. Solid curve refers to I($^2P_{3/2}$) formation, dashed curve to I*($^2P_{1/2}$) formation.

experimentally measured lifetimes of the $HOCO^{\ddagger}$ complex (versus λ_1) since in any theory (statistical or dynamical) a knowledge of the internal energy content of the collision complex is required.

A consideration of great importance in VIB reactions is the initial geometry of the vdW precursor molecule. Central to the concept of precursor geometry-limited reactions is the fact that the constrained geometry affords some measure of steric control of the bimolecular reaction, enabling one to infer something about the orientation dependence of reactivity by comparing, e.g., PSDs from the PGL versus bulk gas phase reaction.

In addition to the steric (angular) limitations imposed by the geometry of the vdW precursor, the range of impact parameters (b) is much reduced relative to the bulk gas or crossed beam bimolecular reaction. In the latter case all impact parameters are sampled and therefore the reaction cross section is given by

$$\sigma_R = \int_0^{\infty} 2\pi b P(b) db, \tag{3}$$

where $P(b)$ is the orientation-averaged reaction probability (the opacity function[3]). In the VIB case only a small range of b, near zero, is available, much as for "half-collisions" in photofragmentation processes.

By analogy with the known linear (equilibrium) structures of the $HF \cdot CO_2$ and $HCl \cdot CO_2$ vdW compounds it was originally assumed by Wittig[13] that $HBr + CO_2$ was also linear, with a structure $BrH \cdots OCO$. (It was recognized that there would be a range of the vdW hydrogen bond angle, with rms amplitude of 20–25 °, based on analogy as above.) Thus they reasoned that the hot H atom was ejected from the HX essentially collinearly toward the OCO, with near-zero impact parameter and orbital angular momentum. Similarly, in our preliminary report on real-time clocking experiments[11] using the $HI \cdot CO_2$ vdW precursor, it was assumed that the UV photolysis of the precursor ensured that the initial H velocity was preferentially directed along the hydrogen bond to the OCO, limiting the range of impact parameters and orienting the reactants.

Subsequent to all of this work on $HBr \cdot CO_2$ and $HI \cdot CO_2$ vdW precursors, Sharpe et al.[49] carried out a high-resolution diode laser (infrared absorption) spectroscopic study of the entire family of $HX \cdot CO_2$ vdW molecules, with surprising results. For $X = F$ and Cl, the structures are linear, as previously found by Klemperer et al.[31] from molecular beam electric resonance experiments and confirmed by the *ab initio* quantum mechanical-electrostatic model computations of Dykstra.[50] However, for $X = Br$ and I, the new IR experiments revealed that the structures are not linear. For $X = Br$, they are T-shaped, much like $Ar \cdot CO_2$, e.g., the C-Br direction is perpendicular to the OCO axis, with the interposed H atom located in one of two equivalent positions off the C-Br line, roughly between the Br and an O atom of the CO_2. (It is believed that the same situation obtains for the $HI \cdot CO_2$ vdW molecule.[49])

Thus the hot H atom is directed to the O atom of the CO_2, but in such a way that the collision can effect a torque on the CO_2, i.e., the HOCO can be formed with non-zero

(initial) angular momentum. In all the earlier VIB papers there had been the assumption that, at least in the most probable collisions of the H with the CO_2, there was essentially zero angular momentum transferred. This was the explanation first given by Wittig et al. to account for the lower average rotational energy of the OH product of the VIB reaction compared to that in the bulk. (Subsequently, Wittig et al.[44] postulated that the lower rotational excitation was due to a lower energy content of the $HOCO^{\ddagger}$ complex; this issue is discussed below.)

What is important for the present purpose is that for the system under investigation, namely, $HI \cdot CO_2$, the precursor molecule geometry is *not* linear, and that the hot H atom + CO_2 collision is definitely *not* a collinear one.

B. Dynamics of the collision complex in real time

As mentioned in Sec. II, we shall use a kinetic model approach to extract the "characteristic times" for the formation and decay of the HOCO collision complex. As a first approximation we consider a simple decay of the $HOCO^{\ddagger}$ to final products, i.e.,

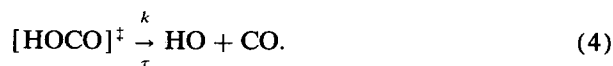$$[HOCO]^{\ddagger} \overset{k}{\underset{\tau}{\to}} HO + CO. \tag{4}$$

Figure 10 shows the results for $\lambda_1 = 256$ nm, together with a fit of the data taking into consideration the above simple exponential rise with proper convolution of the finite pulse widths of our lasers. The dashed curve is the response function determined from the HOOH calibration method, discussed above (the rising exponential is 0.15 ps, convoluted with a 4.5 ps Gaussian pulse). The $t = 0$ position is experimentally fixed, as discussed in Sec. IV. From the fit we obtain $\tau = 5.1$ ps, and this represents the lifetime of $HOCO^{\ddagger}$ at the translational energy dictated by Fig. 9, assuming gas phase bulk behavior. (Even without any assumptions, the raw data show immediately that the lifetime of the $HOCO^{\ddagger}$ is in the picosecond regime.)

The $HOCO^{\ddagger}$, however, is formed following the "collision" between H and CO_2 within the vdW molecule, and it is therefore appropriate to consider the existence of an "induction period" or delay time for HOCO formation. Thus we can represent the overall formation and decay process:

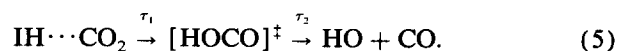$$IH \cdots CO_2 \overset{\tau_1}{\to} [HOCO]^{\ddagger} \overset{\tau_2}{\to} HO + CO. \tag{5}$$

Figure 11 shows the results of the 256 nm experiment, now fitted using the appropriate two-parameter equation (5) for the time-dependence of OH formation. From the best fit, $\tau_1 = 1.2$ ps, $\tau_2 = 4.4$ ps. The apparent induction time (based on the delay in the inflection point) is $\tau_{ind} = 2.1$ ps. These and other representative experimental results are summarized in Table I.

Two points can be noted. First, the value of τ_2 (4.4 ps) is close to τ (5.1 ps), showing that the apparent value for the lifetime of $[HOCO]^{\ddagger}$ is not strongly dependent on the method of analysis of the transient. Also, the measured induction time is consistent with the values of τ_1 and τ_2 since the two-step mechanism dictates the relationship: $\tau_{ind} = \ln(\tau_2/\tau_1)/(\tau_2^{-1} - \tau_1^{-1})$. Second, the fit to the two parameters in Eq. (5) is somewhat better (according to a χ^2

SINGLE RATE FIT; Q1(1), 256nm
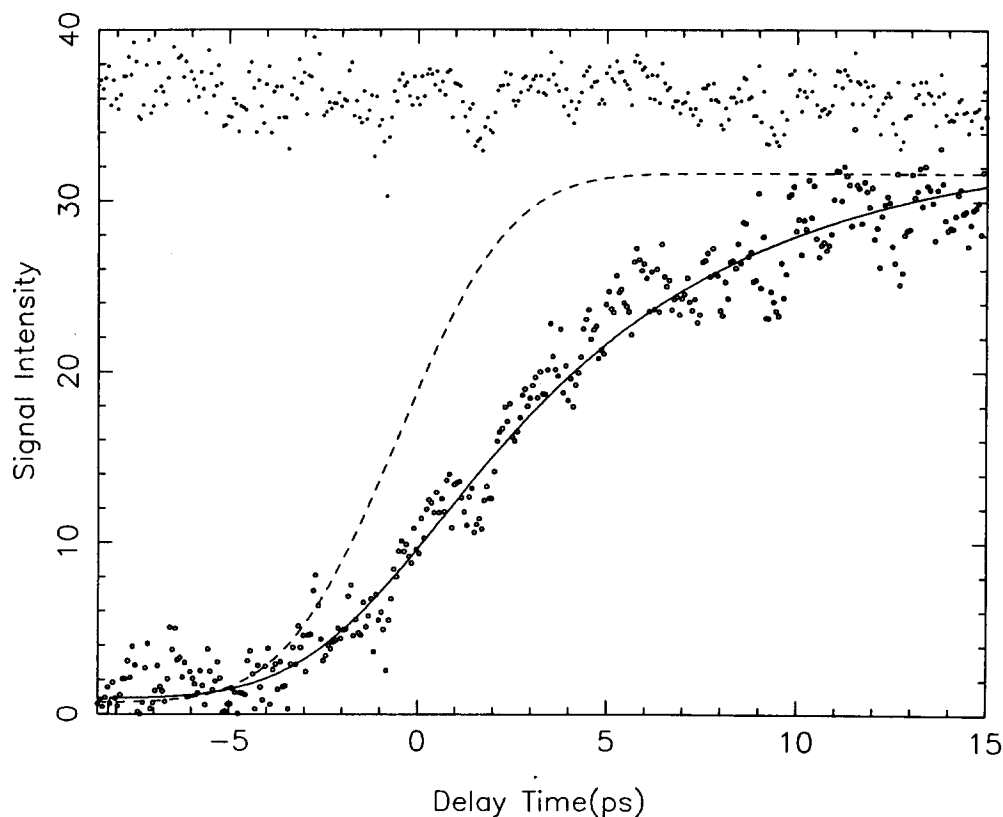

FIG. 10. Plot of representative experimental data on the formation of OH with the VIB reaction from the vdW precursor $HI \cdot CO_2$. Here the pump wavelength $\lambda_1 = 256$ nm. The ordinate is the $Q_1(1)$ LIF signal, proportional to the number density of OH (K = 1), the abscissa the delay time (t_d/ps). The experimental points (small circles) are compared to a theoretical, least-squares best fit (solid curve) obtained by a convolution of an assumed simple, *single* exponential decay of the HOCO‡ (taking a characteristic time $\tau = 5.1$ ps for the formation of OH) with the known pulse shape(s) of the probe (and pump) lasers. The dashed curve is the (integrated) response function of the laser system. The top part of the figure (the points) is a plot of the residuals between the experimental points and the smooth fit.

DUAL RATE FIT; Q1(1), 256nm
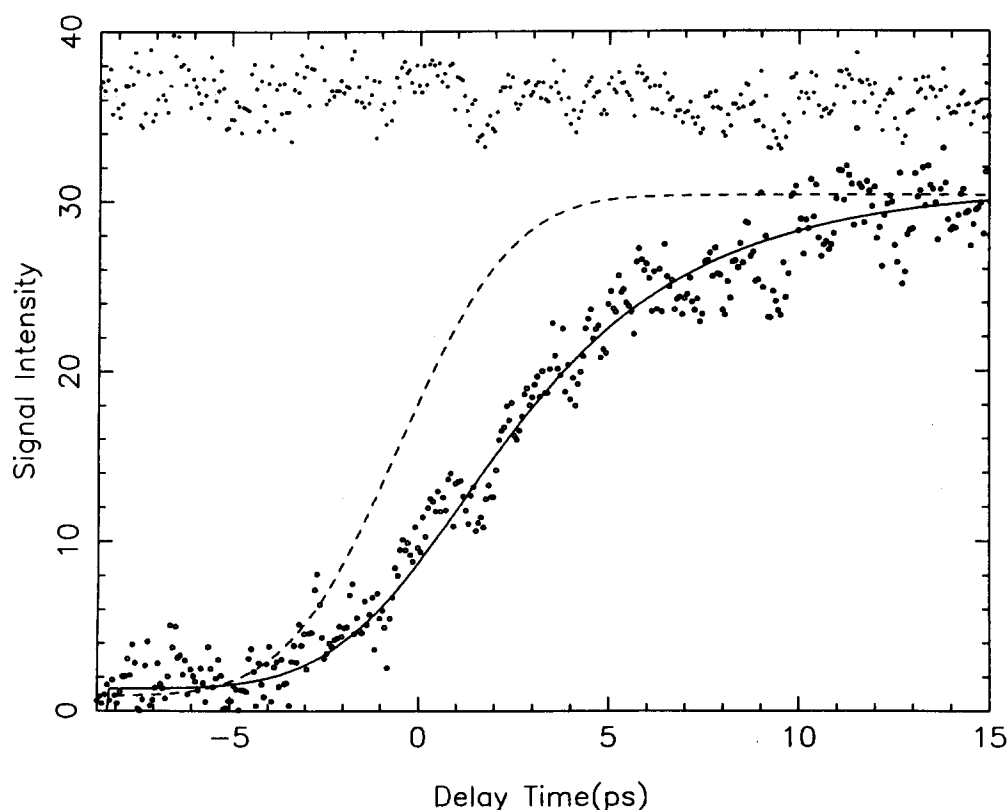
FIG. 11. Plot of the same data as shown in Fig. 10 (the small circles), and the same calculated response function (the dashed curve), but here the solid curve is a calculated best fit (as in Fig. 10) assuming the appropriate two-parameter description [Eq. (5)] of the time dependence of OH formation. The best least-squares fit yielded $\tau_1 = 1.3$ ps, $\tau_2 = 4.7$ ps. The points (top) are the residuals (as in Fig. 10).

TABLE I. Representative examples[a] for the fit parameters for the observed transients of the H + CO_2 VIB reaction. (Entries are times in ps.)

λ	Double exponential fit			Single exponential fit
	τ_1	τ_2	$\Delta\tau_{ind}$	τ
	$Q_1(1)$ detection			
256 nm	1.2	4.4	2.1	5.1
240 nm	1.1	2.4	1.6	2.7
236 nm	0.9	1.9	1.3	2.1
	$Q_1(6)$ detection			
256 nm	1.0	3.8	1.8	4.1
240 nm	0.8	1.6	1.1	1.8
236 nm	0.7	1.1	0.9	1.3

[a] The complete data set for $Q_1(1)$ detection is shown in Fig. 15.

analysis) than the fit to the simple single-exponential of Eq. (4). Figure 12 shows similar results for an independent set of data taken at $\lambda_1 = 240$ nm. However, improvement in S/N is required to establish this point.

To help validate the deduced values of τ_1 and τ_2, we performed computer simulations of the time dependence of OH product concentration using our known temporal response function and values of τ_1 and τ_2 that were obtained from the least-squares fitting of results. These simulation results are shown in Fig. 13 and display features that are very close to the observed experimental results. This gives us more confidence in the experimentally derived values of τ_1 and τ_2. The question is: how do τ_1 and τ_2 change with the pump laser wavelength (λ_1) and thus the available energy, and how do they depend on the rotational state of the OH product? This is addressed in the next sections.

C. Total energy and probe wavelength dependences

In these λ_1-dependence experiments, the detection wavelength for the OH product was kept fixed while varying the pump wavelength. As shown in Fig. 9, the nominal available energy changes according to Eq. (1).

Figure 14 shows three transients obtained at $\lambda_1 = 256$, 240, and 236 nm, all detecting the $Q_1(1)$ transition of the OH. The data show the qualitatively expected behavior, namely, a decrease in both τ_1 and τ_2 as the available energy (E_{avl}) increases. The fit parameters of the data to the scheme of Eq. (5) (i.e., the formation of the HOCO‡ characterized by τ_1 and its decay by τ_2) are listed in Table I. As λ_1 decreases and E_{avl} increases, τ_2 decreases. This is entirely consistent with the idea that as the HOCO‡ internal energy increases, the lifetime of the complex decreases (see below). The complete τ_2 vs λ_1 behavior is shown in Fig. 15. For comparison, we also show the analogous dependence of τ.

At several fixed values of λ_1, the probe wavelength was set to detect a different rotational state of the OH, via the $Q_1(6)$ transition. Figure 16 shows the results for $\lambda_1 = 256$, 240, and 236 nm based on $Q_1(6)$ detection. These results can be compared with those in Fig. 14 for $Q_1(1)$. As discussed below, the results are important in defining the dynamics of the formation and decay of HOCO‡.

D. Discussion of the VIB reaction dynamics: Formation and decay of HOCO

From the results of the present real-time pump-probe study it is clear that the VIB reaction of H + CO_2 proceeds via the "long-lived complex" mode, with the complex presumed to be the HOCO molecule. At the longest pump laser wavelengths for which OH buildup transients were observed, e.g., 263 nm, the decay constant τ_2 of the HOCO‡ is nearly 5 ps. This is comparable to the classical rotation time for CO_2 (HOCO) in its low rotational states (e.g., $J \simeq 8$). [At the shortest wavelengths, e.g., 231 nm (highest HOCO‡ energy), τ_2 was ~1 ps.]

Statistical (RRKM) calculations, as mentioned before, have been carried out by several workers. Various assumptions, as usual, had to be made about the HOCO structure and its intramolecular force field. In all cases it was found that the only way, using simple RRKM formalism, to obtain the experimentally determined "long" lifetimes was to require that the internal energy of the HOCO‡ be lower than the spectator-limit calculated values [from Eq. (1)] by amounts ranging from 10 to 40%. Of course, since all such RRKM calculations are highly dependent upon the structural input parameters, the results are very uncertain. It is not possible to draw quantitative conclusions about the internal excitation level of the HOCO‡ from the observed lifetimes without further work; only the direction of the effect can be ascertained unequivocally. It does *not* appear justified, however, to invoke a bimodal internal energy distribution in the HOCO‡, as assumed recently by Wittig *et al.*[44] in an attempt to explain their relatively cold rotational PSDs for the OH from the HI·CO_2 VIB reaction. Furthermore, it is not obvious that RRKM theory should apply here. Such assumptions can best be tested when HOCO decay is observed directly. It is possible that large deviations like those found in Ref. 25 will be observed here.

Another finding of the present, real-time experiment is the existence of an induction period τ_{ind} for the formation of the HOCO‡, characterized by a time constant τ_1 (with respect to the zero of time defined by the pump laser pulse). As has been discussed, the experimental transients for OH formation are fitted with a two time constant representation, according physically with the scheme:

$$I \sum_{i=0}^{0} \quad H\cdot\cdot C \xrightarrow{\tau_1} HOCO^{\ddagger} \xrightarrow{\tau_2} OH + CO. \qquad (6)$$
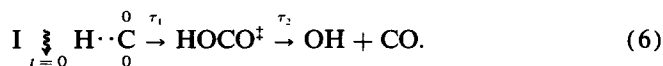
Over the entire pump laser wavelength range (and throughout the range of hot H atom collision energies), τ_1 varied only slightly, declining with E_T from ~1.2 to 0.9 ps ($\pm$ 0.7 ps). The "transit time" for the hot H atom for the few-angstrom transfer to the collision complex, HOCO, is expected to be $\leqslant 0.3$ ps, which would be virtually undetectable with the present temporal resolution. The "extra" time is significantly greater than zero. One concludes that some time, say τ_1, is required to form the "final" isomer of the HOCO (presumably the trans-HOCO), which depends, in turn, upon the energy content of the complex. Some features of the PES in the entrance channel (see, e.g., Fig. 8) should be consis-

DUAL RATE FIT; Q1(6), 240nm

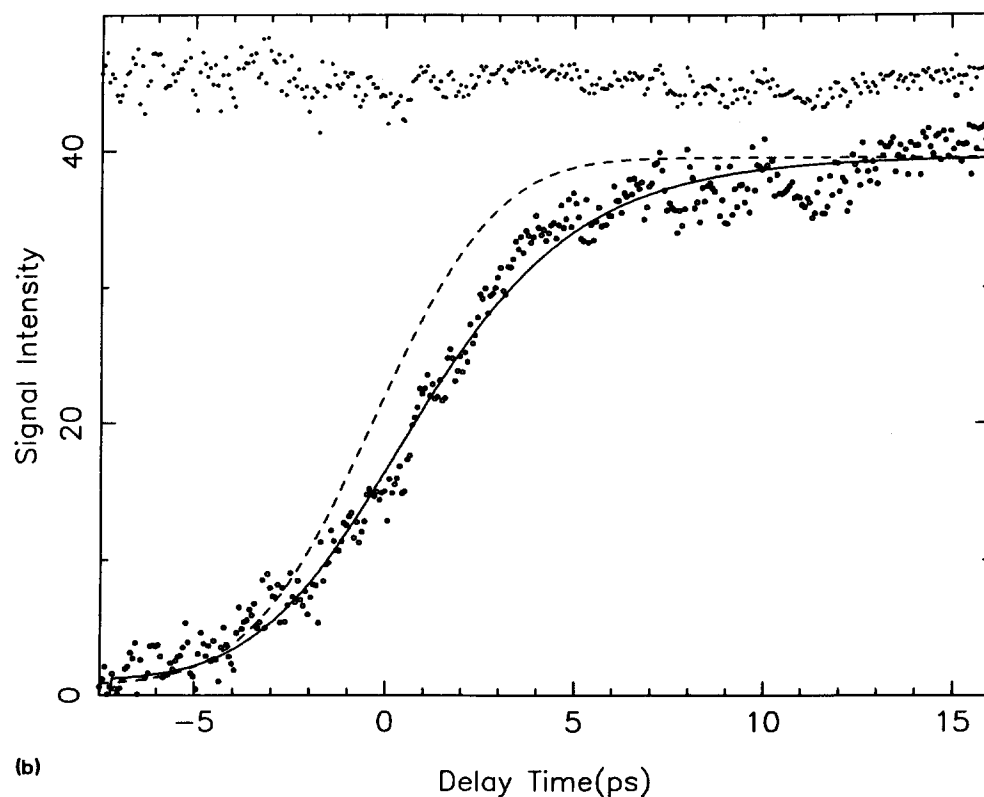**(a)**
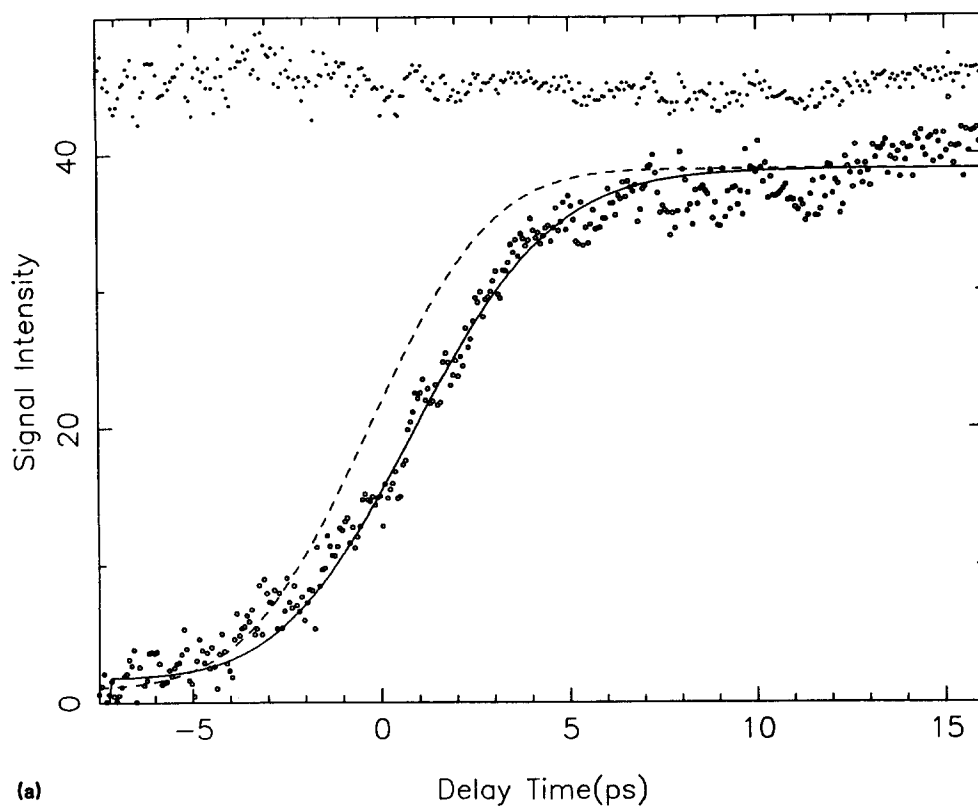
SINGLE RATE FIT; Q1(6), 240nm

(b)

FIG. 12. Plot of a different set of experimental data for a pump wavelength $\lambda_1 = 240$ nm and $Q_1(6)$ LIF detection, i.e., OH ($K = 6$), by the probe laser pulse. As in Fig. 11, the dashed curve is the (integral) response function of the laser system; the small circles are the experimental points. (a) The solid curve here is the convoluted optimal representation of the data assuming a two-parameter description [Eq. (5)]. Best-fit parameters: $\tau_1 = 0.8$ ps, $\tau_2 = 3.8$ ps. Points (top) are residuals (as in Figs. 10 and 11). (b) Here the solid curve is the convoluted, optimal representation with a single exponential (one parameter) description. Best-fit parameter: $\tau_1 = 4.1$ ps.

Simulation of 256nm, Q1(1) Data
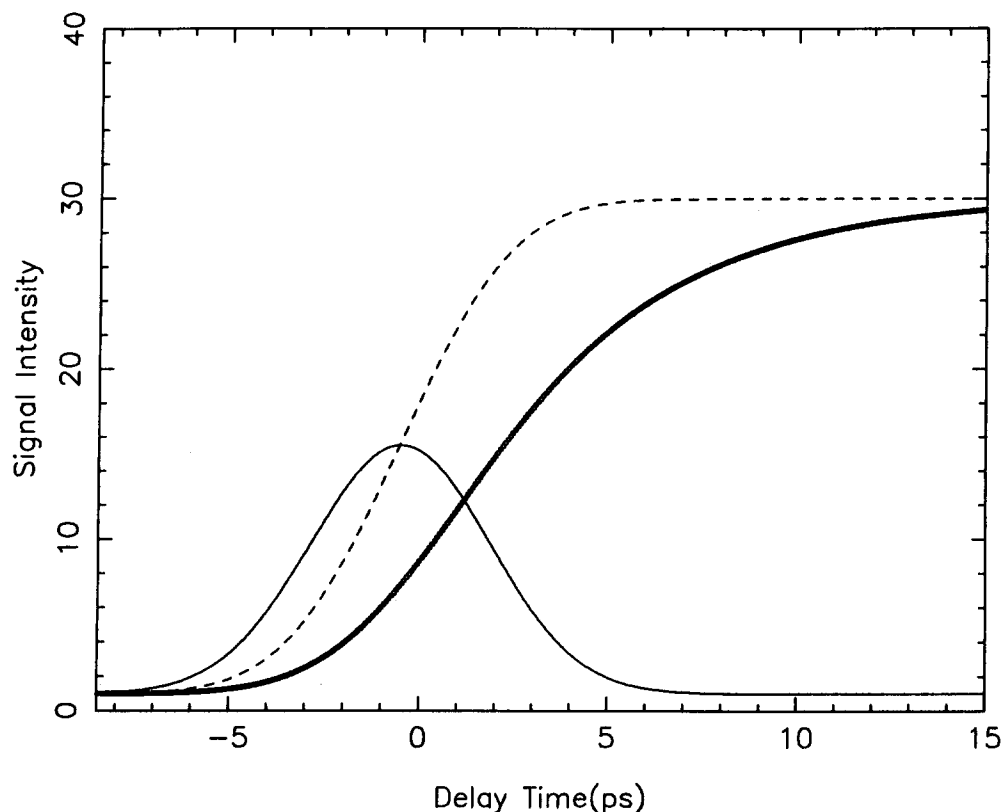
FIG. 13. Results of computer simulation of the experiment corresponding to Fig. 10 [$\lambda_1 = 256$ nm, $Q_1(1)$ detection of OH]. Here the solid curve is a representation of the known temporal shape of the pulsed laser system, the dashed curve the corresponding integrated response function. The smooth, closely spaced set of points represents the convolution, using the τ_1 and τ_2 values from Fig. 10, which should simulate the experimentally observed transient. The agreement is found to be essentially perfect.

DUAL RATE FIT; Q1(1), 256nm
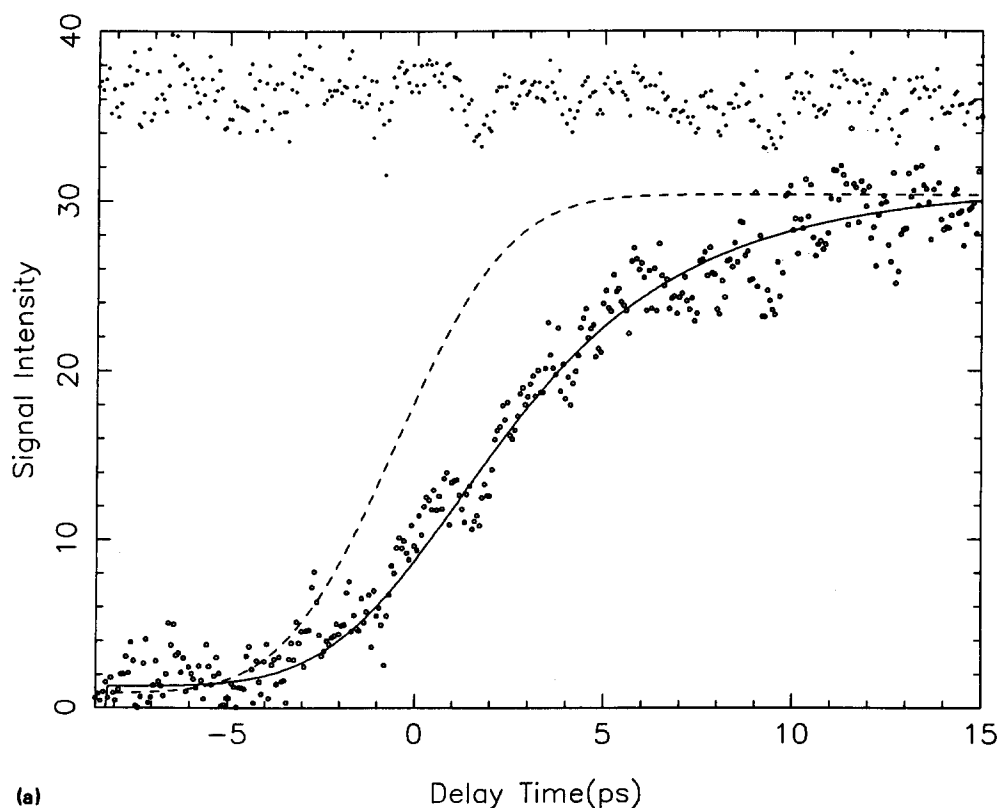
FIG. 14. Experimental results at three different pump laser wavelengths, all with $Q_1(1)$ detection of OH, fitted using the preferred two-parameter representation. The symbols are as in Figs. 10–12. (a) $\lambda_1 = 256$ nm, (b) $\lambda_1 = 240$ nm, (c) $\lambda_1 = 236$ nm. The best-fit parameter sets (τ_1 and τ_2) are listed in Table I.

(a)

DUAL RATE FIT; Q1(1), 240nm

(b)
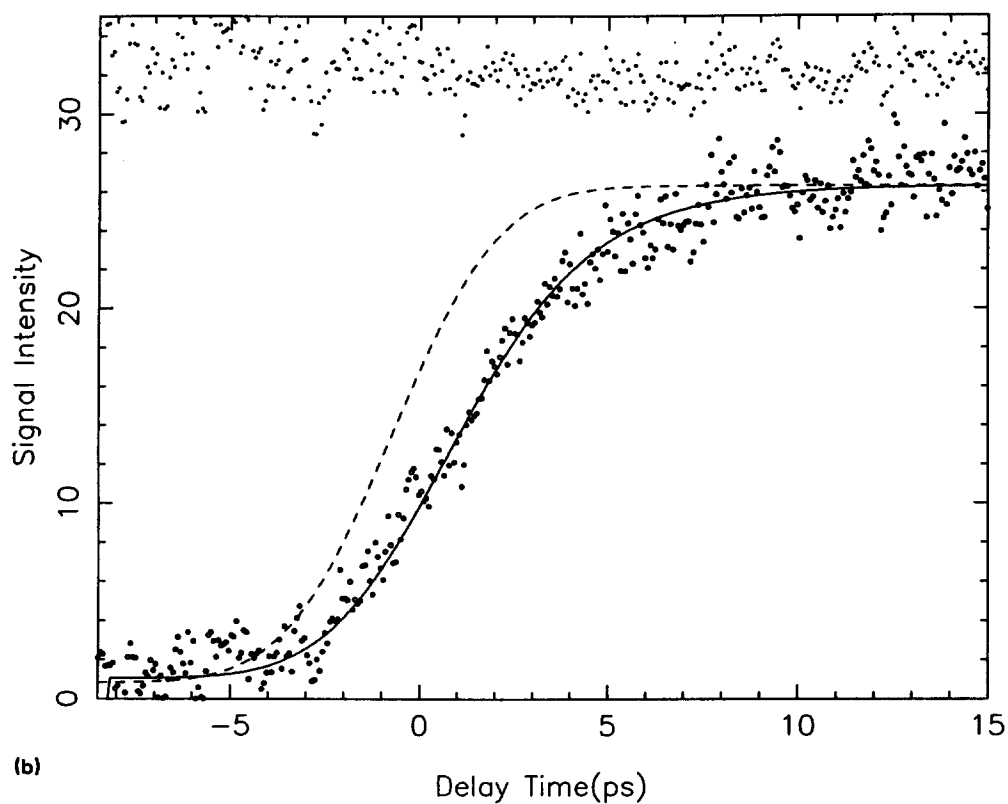
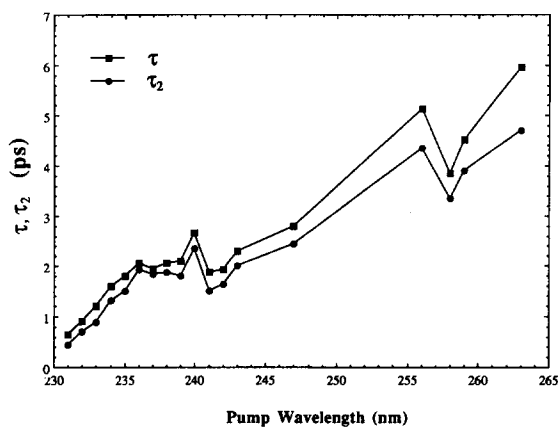## DUAL RATE FIT; Q1(1), 236nm

(c)
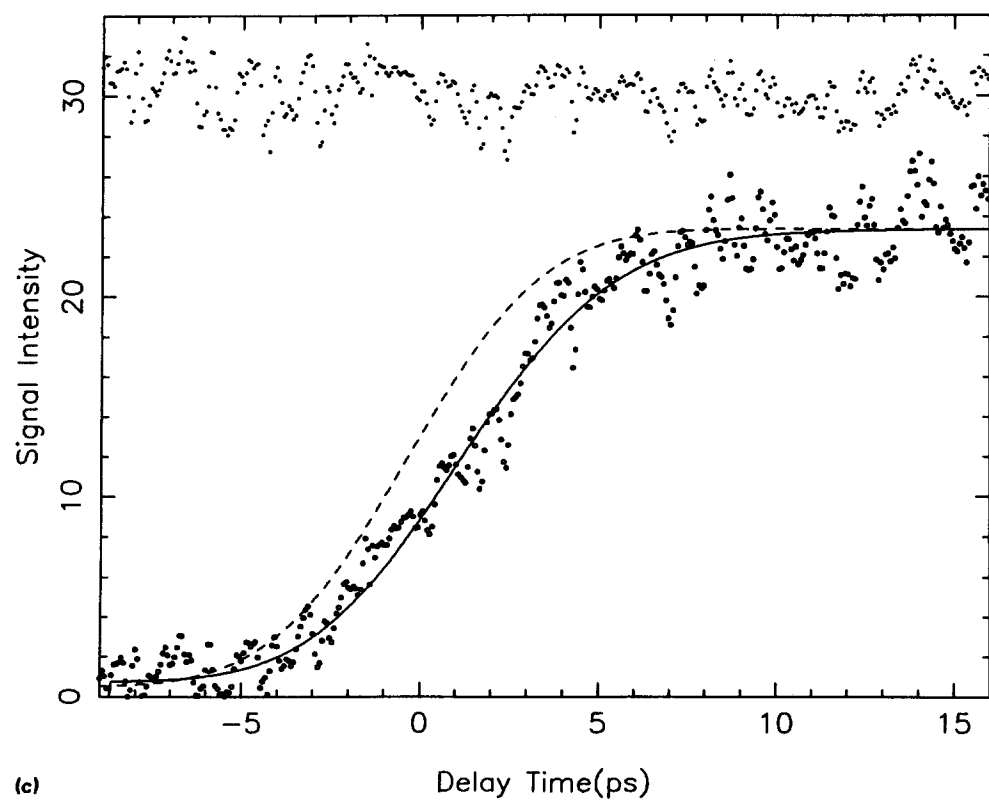
FIG. 15. Global summary of experimental results for $Q_1(1)$ detection, i.e., plot of τ_2 vs pump laser wavelength, λ_1, showing the time constant for the formation of OH ($K = 1$) from HOCO‡ decay as a function of pump wavelength (closely related to the total available energy; see Fig. 9). For completeness, τ (one-parameter fit) as a function of λ_1 is also shown.

tent with this finding. (However, when the femtosecond results on this reaction become available we will be able to quantify the HOCO formation time and have more confidence to relate it to the PES.)

The third significant finding of the present investigation is the dependence of τ_2 upon the rotational state of the OH product, i.e., the shorter HOCO decay constant for $Q_1(6)$ vs $Q_1(1)$ detection. The experiments show that the HOCO molecules which decay to yield OH, $K = 6$ do so significantly faster than those yielding $K = 1$, despite the very small rotational energy difference between these two final states.

(Based on the asymptotic rotational PSD of Wittig *et al.*, the relative probability of formation of the $K = 6$ state is only approximately half of that for $K = 1$.) It is important to note that such a difference in the rate of formation of two product states from the decay of a common precursor, here HOCO, is *not* expected according to simple unimolecular reaction theories. As shown by Khundkar *et al.*,[25] if one initial state of the reaction is involved then the same rate constant should be obtained for all product states. Obviously energetics alone will not suffice to explain these results; angular momentum considerations must play an important role.

Examination of the τ_2 results for $Q_1(1)$ and $Q_1(6)$ detection show a significant deviation from the overall monotonic trend of increasing lifetime with increasing pump wavelength near $\lambda_1 = 240$ nm. The break in the trend is less evident in the $Q_1(6)$ results (not shown). One possible explanation for the change at 240 nm excitation may be the additional contribution to the $Q_1(1)$ detected signal from a second reaction channel. Figure 9 shows the "spectator" energetics for reaction channels corresponding to the I($^2P_{1/2}$) and I($^2P_{3/2}$) final products. The assumed threshold for the H + CO$_2$ reaction is about 104 kJ/mole; a value which is achieved on the I($^2P_{1/2}$)-correlated reaction surface from 240 nm excitation. Of course, the energy deficit of 10–40% which is postulated for reaction on the I($^2P_{3/2}$)-correlated surface would raise the effective threshold unless the effective potential surface for the entrance channel region differs for the I and I* reaction channels. This would indeed be the case if simple additivity of the HI and H + CO$_2$ potential surfaces is sufficient to construct the effective potential for
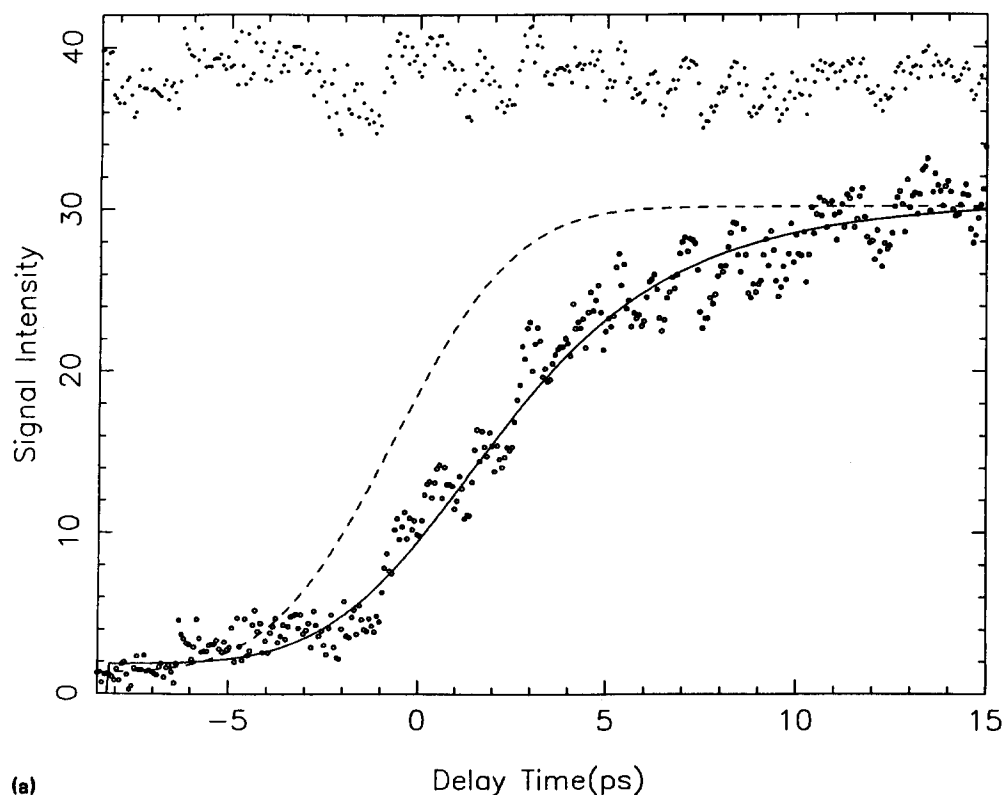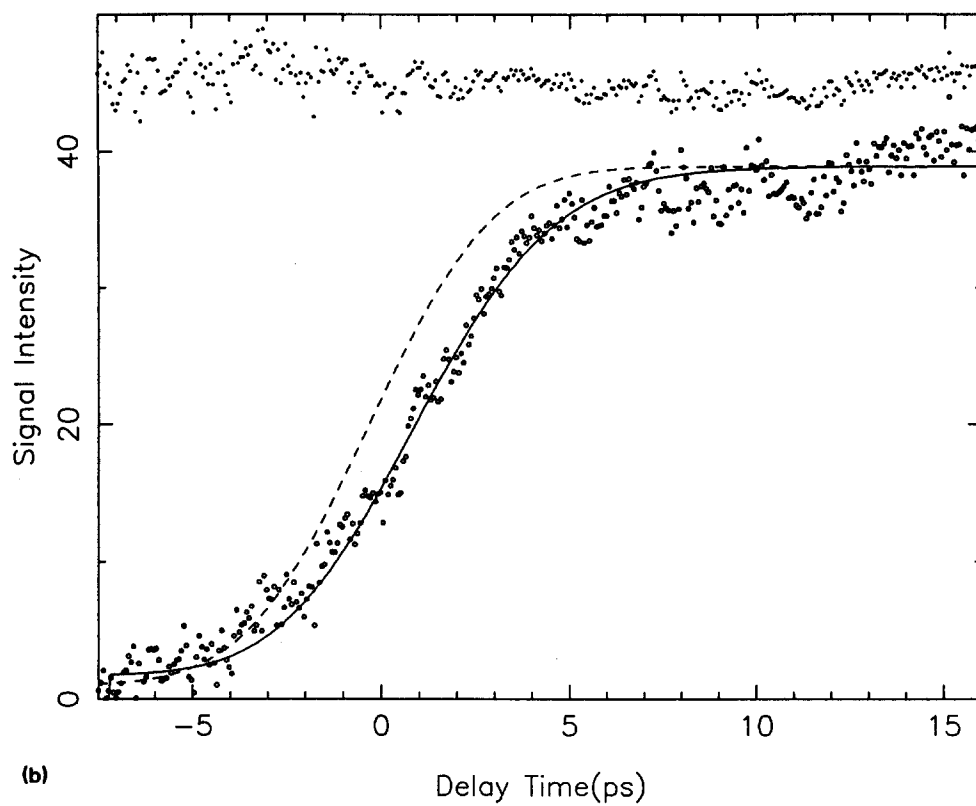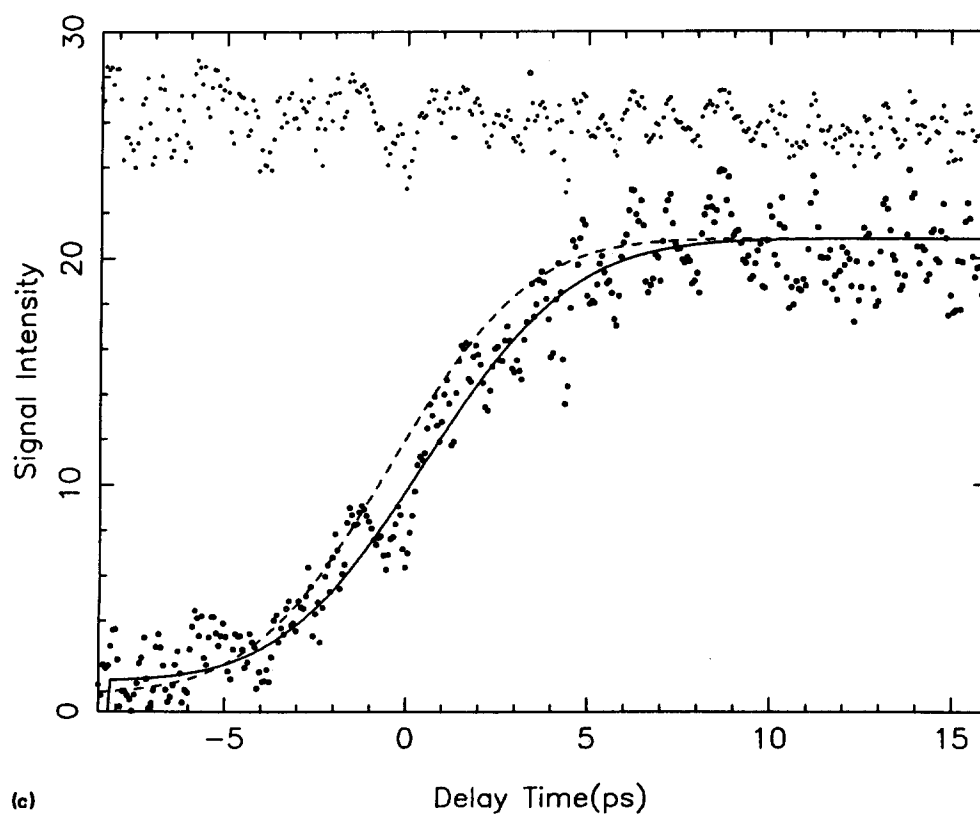
DUAL RATE FIT; Q1(6), 256nm

FIG. 16. Experimental results at three different pump laser wavelengths, all with $Q_1(6)$ detection of OH. Similar presentation as in Fig. 14. (a) $\lambda_1 = 256$ nm, (b)$\lambda_1 = 240$ nm, (c) $\lambda_1 = 236$ nm. Resulting best-fit values of τ_1 and τ_2 are listed in Table I.

(a)   Delay Time(ps)

DUAL RATE FIT; Q1(6), 240nm

(b)

FIG. 16 (*continued*)

DUAL RATE FIT; Q1(6), 236nm

(c)

the reaction. Wilson and coworkers[51] have shown that the $HI \rightarrow H + I(^2P_{1/2})$ repulsive surface is much steeper than that which leads to the $I(^2P_{3/2})$ product.

Now that the structure of the $HI \cdot CO_2$ vdW precursor molecule is known to be nonlinear and the real-time rates of formation and decay of the HOCO collision complex can be measured for the VIB reaction, it is important to undertake definitive theoretical-computational studies of the dynamics, following the approach of Schatz *et al.*[15] What is required is a judicious mix of *ab initio* and semiempirical information to construct an accurate potential energy surface for the vdW precursor, consistent with the best-known equilibrium structure, and that of the HOCO isomers,[52] as well as the vibrational frequencies of the latter (known from the matrix isolation spectra). Then classical calculations should be carried out in the same spirit as for the "half-collision" systems, e.g., $ICN \rightarrow I + CN$, starting from the $HI \cdot CO_2$ precursor, photofragmenting the HI, following the H atom attack on the CO_2 to form the HOCO collision complex, and witnessing its eventual decay to OH + CO. Such calculations should lead to estimates of τ_1 and τ_2 as a function of pump laser wavelength, i.e., the factor determining the energy content of the $HOCO^{\ddagger}$. The ultimate goal is to recover not only the temporal behavior (τ_1 and τ_2) of the present investigation but also the asymptotic PSDs as a function of λ_1.

VI. FINAL REMARKS

The main conclusion of the present study is that real-time measurements of the formation and decay of collision complexes in bimolecular reactions *can* be made. The van der Waals-impacted bimolecular (VIB) reaction of $H + CO_2$ has been the demonstration system illustrating the methodology. Real-time measurements of the rate of the decay of the HOCO intermediate complex for this reaction have been made over a wide range of collision energies. With FTS methods, it should be possible to observe the transition states of VIB reactions and ultimately to extend the field of *femtochemistry* to a large class of elementary bimolecular reactions.

ACKNOWLEDGMENTS

[1] For a review, see A. H. Zewail, Science **242**, 1645 (1988); A. H. Zewail and R. B. Bernstein, C&E News **66**, 24 (1988).

[2] D. R. Herschbach, Angew. Chem. Int. Ed. Engl. **26**, 1221 (1987).

[3] See, e.g., R. D. Levine and R. B. Bernstein, *Molecular Reaction Dynamics and Chemical Reactivity* (Oxford University, New York, 1987).

[4] P. Brumer and M. Karplus, Faraday Discuss. Chem. Soc. **55**, 80 (1973).

[5] See Ref. 3 for more details.

[6] C. E. Klots, J. Phys. Chem. **75**, 1526 (1971); S. A. Safron, N. D. Weinstein, D. R. Herschbach, and J. C. Tully, Chem. Phys. Lett. **12**, 564 (1972); M. Quack and J. Troe, Ber. Bunsenges Phys. Chem. **78**, 240 (1974); **79**, 170 (1975); R. A. Marcus, J. Chem. Phys. **62**, 1372 (1975); G. Worry and R. A. Marcus, J. Chem. Phys. **67**, 1636 (1977); J. C. Light in *Atom-Molecule Collision Theory*, edited by R. B. Bernstein (Plenum, New York, 1979), p. 647.

[7] A. M. Ding, L. J. Kirsch, D. S. Perry, J. C. Polanyi, and J. L. Schreiber, Faraday Discuss. Chem. Soc. **55**, 252 (1973).

[8] H. W. Cruse, P. J. Dagdigian, and R. N. Zare, Faraday Discuss. USS. Chem. Soc. **55**, 277 (1973).

[9] J. M Farrar and Y. T. Lee, Annu. Rev. Phys. Chem. **25**, 357 (1974).

[10] R. Altkorn and R. N. Zare, Annu. Rev. Phys. Chem. **35**, 265 (1984).

[11] N. F. Scherer, L. R. Khundkar, R. B. Bernstein, and A. H. Zewail, J. Chem. Phys. **87**, 1451 (1987).

[12] C. Jouvet and B. Soep, J. Chem. Phys. **80**, 2229 (1984); Chem. Phys. Lett. **96**, 426 (1983).

[13] S. Buelow, G. Radhakrishnan, J. Catanzarite, and C. Wittig, J. Chem. Phys. **83**, 444 (1985); G. Radhakrishnan, S. Buelow, and C. Wittig, *ibid.* **84**, 727 (1986); S. Buelow, M. Noble, G. Radhakrishnan, H. Reisler, C. Wittig, and G. Hancock, J. Phys. Chem. **90**, 1015 (1986).

[14] C. Wittig, S. Sharpe, and R. A. Beaudet, Acc. Chem. Res. **21**, 341 (1988).

[15] G. C. Schatz, M. S. Fitzcharles, and L. B. Harding, Faraday Discuss. Chem. Soc. **84**, 359 (1987); G. C. Schatz and M. S. Fitzcharles, in *Selectivity in Chemical Reactions*, edited by J. C. Whitehead (Kluwer Academic, Dordrecht, The Netherlands, 1988), p.353.

[16] D. R. Herschbach, Faraday Disc. Chem. Soc. **55**, 233 (1973).

[17] M. J. Rosker, M. Dantus, and A. H. Zewail, J. Chem. Phys. **89**, 6113 (1988); M. Dantus, M. J. Rosker, and A. H. Zewail, *ibid.* **89**, 6128 (1988); R. B. Bernstein and A. H. Zewail, *ibid.* **90**, 829 (1989); T. Rose, M. J. Rosker, and A. H. Zewail, *ibid.* **91**, 7415 (1989); M. Dantus, R. Bowman, M. Gruebele, and A. H. Zewail **91**, 7437 1989); and reference therein.

[18] P. M. Felker and A. H. Zewail, Adv. Chem. Phys. **70**, 265 (1988).

[19] J. L. Knee, L. R. Khundkar, and A. H. Zewail, J. Chem. Phys. **87**, 115 (1987); D. H. Semmes, J. S. Baskin, and A. H. Zewail, J. Am. Chem. Soc. **109**, 4104 (1987); D. H. Semmes, J. S. Baskin, and A. H. Zewail, J. Chem. Phys. **92**, 3359 (1990).

[20] F. Lahmani, A. Tramer, and C. Tric, J. Chem. Phys. **60**, 4431 (1974).

[21] S. O. Williams and D. G. Imre, J. Phys. Chem. **92**, 6648 (1988); V. Engel, H. Metiu, R. Almeida, R. A. Marcus, and A. H. Zewail, Chem. Phys. Lett. **152**, 1 (1988); S. E. Choi and J. C. Light, J. Chem. Phys. **90**, 2593 (1989); M. Gruebele, G. Roberts, and A. H. Zewail, Philos Trans. Roy. Soc., London (in press).

[22] A. H. Zewail, Faraday Trans. Chem. Soc. 2 **85**, 1221 (1989).

[23] M. Dantus, R. M. Bowman, J. S. Baskin, and A. H. Zewail, Chem. Phys. Lett. **159**, 406 (1989).

[24] H. M. Crosswhite and G. H. Dicke, J. Quant. Spec. Radiat. Trans. **2**, 97(1964); I. L. Chidsey and D. R. Crosley, *ibid.* **23**, 187 (1980); W. L. Dimpfl and J. L. Kinsey, *ibid.* **21**, 233 (1979).

[25] L. R. Khundkar, J. L. Knee, and A. H. Zewail, J. Chem. Phys. **87**, 77 (1987); N. F. Scherer and A. H. Zewail, *ibid.* **87**, 97 (1987); J. L. Knee, L. R. Khundkar, and A. H. Zewail, *ibid.* **87**, 115 (1987); E. Potter, M. Gruebele, and A. H. Zewail, Chem. Phys. Lett. **164**, 463 (1989).

[26] T. Jimbo, V. L. Caplan, Q. X. Li, Q. Z. Wang, P. P. Ho and R. R. Alfano, Opt. Lett. **12**, 477 (1987); R. L. Fork, C. V. Shank, C. Hirlmann, R. Yen, and W. J. Tomlinson, *ibid.* **618**, 1 (1983).

[27] R. R. Alfano, L. L. Hope, and S. L. Shapiro, Phys. Rev. A **6**, 433 (1972); C. X. Li, T. Jimbo, P. P. Ho, and R. R. Alfano, Appl. Opt. **25**, 1869 (1986).

[28] O. E. Martinez, IEEE J. Quantum Electron. **QE-23**, 59 (1987).

[29] E. B. Treacy, IEEE J. Quantum Electron. **QE-5**, 454 (1969).

[30] B. W. Keelan, J. A. Syage, J. F. Shepanski, and A. H. Zewail, *Int. Conf. Lasers* (STS, McLean, VA, 1985), p. 718.

[31] F. A. Baiocchi, T. A. Dixon, C. H. Joyner, and W. Klemperer, J. Chem. Phys. **74**, 6544 (1981).

[32] L. R. Khundkar, Ph. D. thesis, California Institute of Technology, 1988.

[33] W. C. Wiley and I. H. McLaren, Rev. Sci. Instrum. **26**, 1150 (1955).

[34] N. F. Scherer, J. L. Knee, D. D. Smith, and A. H. Zewail, J. Phys. Chem. **89**, 5141 (1985); N. F. Scherer, Ph. D. thesis, California Institute of Technology, 1989.

[35] G. A. Oldershaw and D. A. Porter, Nature **223**, 490 (1969).

[36] R. E. Tomalesky and J. E. Sturm, J. Chem. Soc. Far. Trans. 2 **68**, 1241 (1972).

[37] C. R. Quick and J. J. Tiee, Chem. Phys. Lett. **100**, 223 (1983).

[38] K. Kleinermanns and J. Wolfrum, (a) Laser Chem. **2**, 339 (1983); (b) Chem. Phys. Lett. **104**, 157 (1984); (c) K. Kleinermanns, E. Linnebach, and J. Wolfrum, J. Phys. Chem. **89**, 2525 (1985); (d) A. Jacobs, M. Wahl, R. Weller, and J. Wolfrum, Chem. Phys. Lett. **158**, 161 (1989).

[39] J. F. Herschberger, S. A. Hewitt, S. K. Sarkar, and G. W. Flynn, J. Chem. Phys. **91**, 4636 (1989); G. W. Flynn, Science **246**, 1009 (1989).

[40] For a review, see G. W. Flynn and R. E. Weston, Jr., Annu. Rev. Phys. Chem. **37**, 551 (1986).

[41] I. W. M. Smith and R. Zellner, J. Chem. Soc. Faraday Trans. 2 **69**, 1617 (1973); I. W. M. Smith, Chem. Phys. Lett. **49**, 112 (1977); J. Brunning, D. W. Derbyshire, I. W. M. Smith, and M. D. Williams, J. Chem. Soc. Faraday Trans. 2 **84**, 105 (1988).

[42] C. W. Larson, D. H. Stewart, and D. M. Golden, Int. J. Chem. Kinetics **20**, 27 (1988); D. M Golden, J. Chem. Phys. **83**, 108 (1977).

[43] M. Mozurkewich, J. J. Lamb, and S. W. Benson, J. Phys. Chem. **88**, 6435 (1984).

[44] Y. Chen, G. Hoffmann, D. Oh, and C. Wittig, Chem. Phys. Lett. **159**, 426 (1989); G. Hoffmann, D. Oh, Y. Chen, Y. M. Engel, and C. Wittig, Isr. J. Chem. (in press).

[45] N. F. Scherer, Ph. D. dissertation, California Institute of Technology, 1989.

[46] C. Wittig, Y. M. Engel, and R. D. Levine, Chem. Phys. Lett. **153**, 411 (1988).

[47] D. E. Milligan and M. E. Jacox, (a) J. Chem. Phys. **54**, 927 (1971); (b) M. E. Jacos, J. Chem. Phys. **88**, 4598 (1988).

[48] C. Sipes, M. Sc. thesis, California Institute of Technology, 1988.

[49] S. W. Sharpe, Y. P. Zeng, C. Wittig, and R. A. Beaudet, J. Chem. Phys. (in press).

[50] For a review, see C. E. Dykstra, *Ab Initio Calculation of the Structures and Properties of Molecules* (Elsevier, Amsterdam, 1988), pp. 79–85.

[51] R. D. Clear, S. J. Riley, and K. R. Wilson, J. Chem. Phys. **63**, 1340 (1975).

[52] A. D. McLean and Y. Ellinger, Chem. Phys. **94**, 25 (1985).